3D MACROELEMENT APPROACH FOR NONLINEAR FE ANALYSIS OF URM COMPONENTS SUBJECTED TO IN-PLANE AND OUT-OF-PLANE CYCLIC LOADING

E. Minga[1], L. Macorini[1], B.A. Izzuddin[1] and I. Calio'[2]

[1]Department of Civil and Environmental Engineering, Imperial College London, UK
[2]Department of Civil Engineering and Architecture, University of Catania, Italy

Abstract

The paper presents a novel 3D macroelement approach for efficient and accurate nonlinear analysis of unreinforced masonry components subjected to in-plane and out-of-plane cyclic loading. A macroscopic description for masonry is employed, where macroelements, consisting of deformable blocks interacting through cohesive interfaces, are used to represent large portions of masonry walls, enhancing computational efficiency. Enriched kinematic characteristics are adopted for the homogeneous blocks, where in-plane shear and out-of-plane bending modes are described by two independent Lagrangian parameters. Moreover, a detailed material model for the nonlinear interfaces connecting adjacent elements enables an accurate representation of complex failure modes and cracking patterns in masonry walls. As a result, the proposed FE strategy can be employed for accurate response predictions of large masonry structures subjected to cyclic loading conditions. The accuracy of the macroelement approach is validated through comparisons against results of experimental tests of solid and perforated masonry walls under in-plane and out-of-plane loading.

Keywords: Unreinforced masonry; nonlinear analysis; in-plane and out-of-plane cyclic loading; finite element method; 3D macroelement; mixed-mode failure.

1 Introduction

Unreinforced masonry (URM) has been used in the construction of buildings, bridges and monuments for centuries. Historical masonry structures form an important part of the cultural and engineering heritage. Masonry is also employed in modern structures, mainly for secondary components, such as infill panels in buildings with steel or concrete frames, and for the load bearing elements of low-rise buildings for its reduced cost and remarkable durability. As a result, at present there is a significant interest in the assessment of the structural integrity of URM components and structures and their vulnerability against various hazards, including earthquakes.

An accurate prediction of the response of URM components under general loading conditions can be achieved using detailed models explicitly accounting for the mesostructure of the material. Such mesoscale descriptions, which can be developed within the finite element (FE) framework [1, 2, 3] or utilising discontinuum approaches like the discrete element method (DEM) [4, 5, 6] are also associated with convenient calibration of material properties by simple component tests on units and mortar joints [7]. This is particularly relevant when assessing the performance of existing structures, where low invasive in-situ tests can be employed for the identification of material model parameters [8]. On the other hand, mesoscale models, especially when based on 3D representations of masonry materials with small units, require prohibitive computational cost and an excessively time-consuming pre-processing stage. Computational efficiency can be enhanced utilising partitioning strategies and parallel computation resources [9, 10] or multi-scale approaches [11, 12, 13] which improve the potential of using detailed modelling for the analysis of URM structures, though even such advanced strategies are computationally demanding when applied to large-scale structural systems. Thus, when employing conventional computational resources their scope of applicability is restricted to the analysis of small masonry components. As a result, more efficient, hence less detailed, macroscopic descriptions are necessary, especially for the investigation of the nonlinear response of large masonry structures subjected to extreme conditions as in the case of earthquake loading. For the modelling of such structures, URM is typically represented as a homogeneous material at structural scale, and its macroscopic behaviour is described in a phenomenological way. In general, the identification of macroscale material parameters is conducted at the structural component level, as macroscale models allow for masonry bond only implicitly. Thus, the influence of masonry texture is inherently related to the definition of the macroscale material properties, which can be determined by expensive and invasive in-situ experiments [14] or from mesoscale simulations using homogenisation techniques [15, 16, 17] and multi-level calibration procedures [18].

In the main, two approaches can be identified within the masonry macroscale framework. The first one consists in the use of shell or solid finite elements with 2D or 3D plastic damage constitutive laws describing the macroscopic behaviour of URM [19, 20, 21]. The main advantages of this strategy are the flexibility in the description of complex geometries and the relative computational efficiency when compared to micro- or mesoscale modelling approaches. However, there are limitations related to the representation of damage as a smeared material characteristic within a certain volume, and to the ability to predict realistic cracking patterns and failure mechanisms in masonry components with complex texture (e.g. multi-leaf walls) subjected to generic loading conditions.

The second approach for macroscale modelling of URM structures is based on the use of sets of basic mechanical components, such as nonlinear springs or beams, which are properly arranged to form macroelements. In most cases, each macroelement accounts for material nonlinearity using phenomenological constitutive models to describe the macroscopic nonlinear response of the modelled structural component under specific deformation modes. Among existing macroelement strategies, the Equivalent Frame Approach, EFA [22, 23, 24] is widely used for its simplicity and computational efficiency. It is based on the assumption that the piers and/or the spandrels of masonry buildings can be represented by 1D macroelements with concentrated plasticity, while rigid offsets are used to connect distinct members. Despite the clear advantages, including the possibility to practically allow for strength and stiffness degradation under cyclic loading [25], standard EFAs have certain limitations, including geometrical inconsistency, the very crude representation of the interaction between structural members, the difficulty in modelling complex geometries and the lack of representation of out-of-plane failure modes.

2D or 3D macroelements offer an alternative strategy that might tackle certain of those limitations, while maintaining the computational efficiency essential for nonlinear static and dynamic analysis. A strut-and-tie model was proposed by [26], which draws an equivalence between the in-plane behaviour of URM panels and a system of articulated struts with elastic-perfectly plastic response in compression and zero tensile resistance. The model, which had been previously used to represent concrete walls, can reproduce in a distinct, albeit rather abstract way, diagonal shear or flexural failure; however, its extension to 3D is not straightforward. Other approaches are based on 2D or 3D rigid elements connected through springs to reproduce the macroscopic behaviour of a unit cell of the URM assembly. These include the Rigid Body Spring Model proposed by [27] utilising uncoupled axial and shear springs calibrated based on assumed failure mechanisms within a unit cell of URM, which is considered a heterogeneous periodic material. The model, which has been conceived for dynamic analysis, shows computational benefits due to its simplicity and the ability to reproduce the in-plane flexural, diagonal shear and compressive crushing failure modes of masonry. However, the adopted simplified constitutive laws overestimate the hysteretic energy dissipation in the case of rocking. Moreover, mechanisms that follow other than the assumed failure patterns might not be well represented. A similar strategy was employed in [28] for investigating the in-plane URM behaviour and in the modelling approach put forward by [29] for the out-of-plane URM response. In this case, homogenisation principles are employed to derive holonomic constitutive laws for the springs connecting the rigid elements. These laws are derived in an independent step, and then used within standard commercial FE software providing efficiency in the structural analysis. However, they do not yet account for the cyclic response of masonry. Caliò et al. [30] proposed a discrete plane element that also includes shear deformation modes for the homogeneous block, thus including the possibility to represent diagonal shear cracking with a reduced number of elements. This approach was extended to represent the 3D behaviour [31, 32] incorporating into a single macro-element the in-plane and out-of-plane response.

The present work assumes a description of URM through 3D homogeneous blocks connected through cohesive/frictional interfaces. It thus enables the realistic modelling of any URM structure with openings, properly accounting for the interaction between the different structural components. Instead of uncoupled springs, the blocks in the present approach interact based on a sophisticated 3D material description for zero-thickness cohesive interfaces which directly couples the normal with the tangential behaviour. In addition, the kinematics of the homogeneous block includes an in-plane shear deformation mode, as well as an out-of-plane diagonal bending mode. These modes allow the representation of in-plane and out-of-plane failure modes associated with diagonal cracking of URM components within a single macroelement. As a result, all the principal failure modes of components of URM buildings can be represented with a reduced number of elements, increasing the computational efficiency. As opposed to previous macroelement strategies (e.g. [30, 31, 32]), the proposed macroelement approach had been developed within a FEM framework with flexible connectivity with adjacent elements through its four boundary edges which represents a distinctive feature. This facilitates its combination with different types of finite elements, including quadratic beams and shells and the use of the capabilities of standard FEM software packages.

2 Macroelement representation of URM

2.1 Assumptions and macroelement characteristics

The main objective of the developed macro-element is to provide an efficient and accurate representation of the typical in-plane and out-of-plane failure modes including i) diagonal shear cracking (Figure 1a), ii) shear sliding (Figures 1b,f), iii) flexural cracking (Figures 1c,e), iv) toe crushing (Figure 1d) and v) diagonal cracking under two-way bending (Fig. 1g), which typically develop in URM components of buildings under earthquake loading.

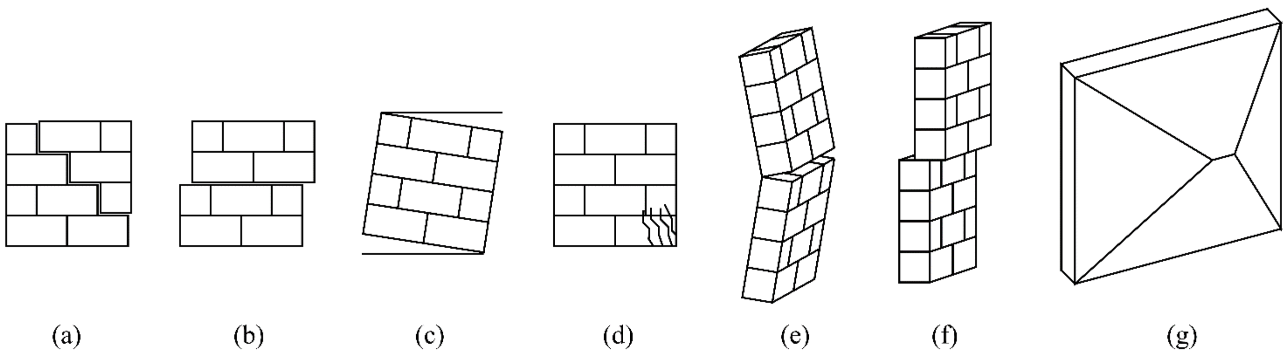

Figure 1. Failure modes of URM components: (a)-(d) in-plane and (e)-(g) out-of-plane

To achieve a good balance between accuracy and computational efficiency, the macro-element is designed to represent the nonlinear behaviour at the scale of an entire masonry component (e.g pier or spandrel) or of a substantial part of it that generally consists of an assembly of several brick/block units and mortar joints. The onset of each failure mode is controlled through commonly used macroscopic or phenomenological material parameters, such as the flexural strength and the shear strength of masonry, which can be estimated by physical experiments or virtual tests by employing detailed micro- or mesoscale descriptions [18].

The proposed element formulation is based on a 3D continuum rectangular block, which represents in a macroscopic homogeneous way a rectangular part of a URM component. The block interacts with adjacent elements through cohesive interfaces along four of its faces, as shown in Figure 2a. As a result, it enables a realistic representation of any plane geometry with arbitrary openings. The inner block has two specific deformation modes: in-plane shear deformation, as shown in Figure 2b, and out-of-plane diagonal bending deformation, as depicted in Figure 2c, but is otherwise rigid. The two deformation modes are governed by a single Lagrangian parameter that is represented by two nonlinear springs, sketched in Figures 2b and 2c, representing, in a phenomenological way, the main collapse mechanisms of a masonry wall component which cannot be described by damage in the surrounding interfaces. The shear mode allows the reproduction of diagonal shear cracking of masonry (Figure 1a) while the out-of-plane deformation enables the simulation of diagonal cracking due to flexure out-of-plane (Figure 1g). In the macro-element proposed by Pantò el al. [31, 32], the latter out-of-plane mechanism cannot be reproduced in a single element and a larger number of elements is needed for a suitable simulation of the out-of-plane response. The incorporation of the out-of-plane deformation mode allows the description of this effect with the use of much coarser meshes. Obviously, the number of elements necessary for each case is conditional to the geometry of the wall and the presence of openings.

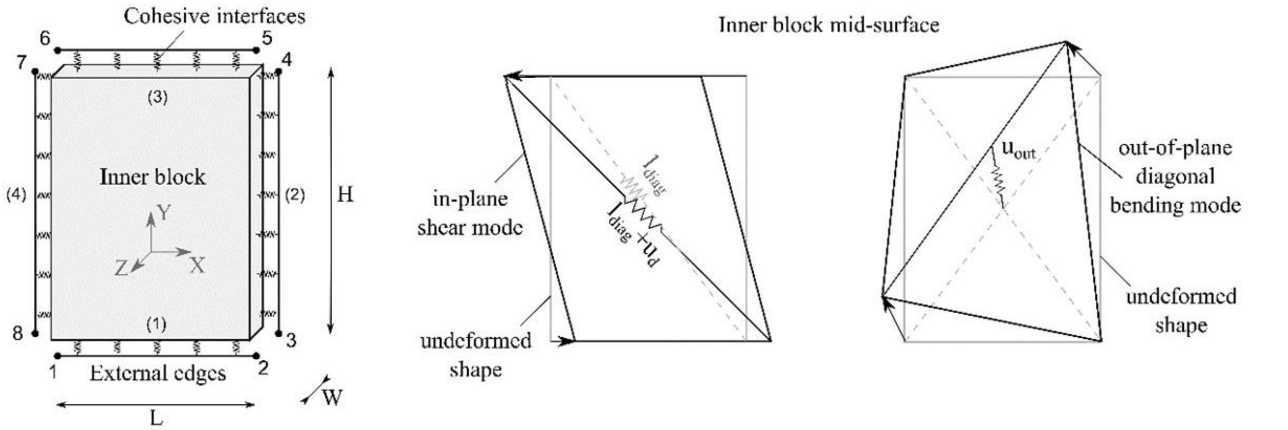

(a) (b) (c)

Figure 2. (a) URM macroelement; (b) In-plane shear deformation mode of inner block; (c) Out-of-plane diagonal bending mode of inner block

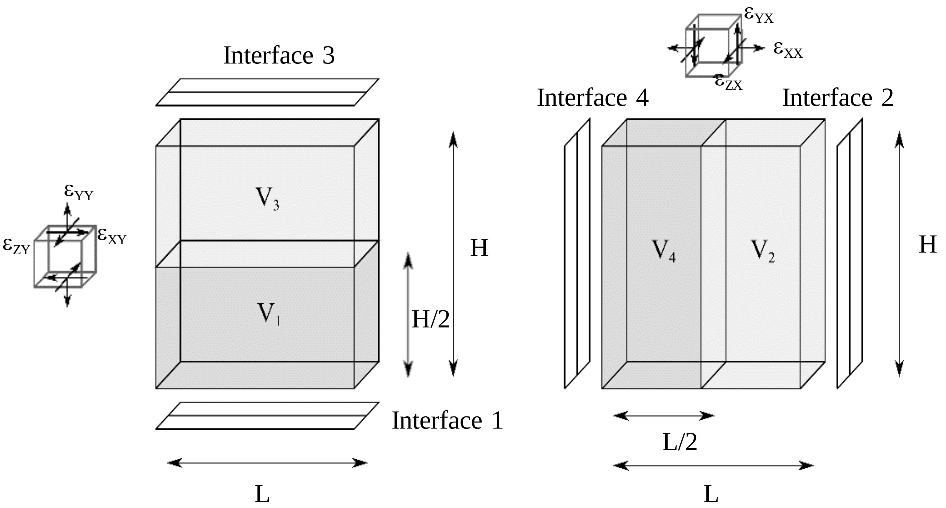

Figure 3. Areas of influence of the interfaces between the inner block and the external edges

Zero-thickness interfaces are defined along the four macroelement boundaries, as illustrated in Figure 2a. It is assumed that all normal elastic in-plane deformation within the masonry block is concentrated along these interfaces, based on the influence areas related to the corresponding volumes as shown in Figure 3. In a similar way, shear sliding (Figure 1b) and tensile damage within the block (Figure 1c) are represented by tensile or shear damage concentrated along the corresponding interfaces. Additionally, the effect of toe crushing (Figure 1d) can be accounted for by defining an ultimate compressive strength along the interfaces. Hence, on the whole, the 3D macroelement can reproduce all the collapse mechanisms of a URM panel shown in Figure 1.

2.2 Connectivity

The element connectivity is defined through the eight nodes of the external edges. The order of connectivity is shown in Figure 2a. The pairs of nodes at the corners (2-3,4-5,6-7,8-1) have the same coordinates, but are sketched some distance apart for clarity. Two possibilities have been considered, which correspond to different modelling requirements for different types of structures:

- In the first case, the corners between the element edges are defined by two distinct nodes. This configuration is chosen when modelling URM structures and URM blocks which are connected to each other. In this case, the external edges represent a fictional boundary between two parts of the URM structure and they do not transfer moments, allowing for a linear variation of the normal relative displacement and sliding along the horizontal and vertical edges of the macro-element. Figure 4a shows an example of this type of connectivity.
- In the second case, a corner consists of a single node. In this setting, the two adjacent edges share the displacements and rotations at this node. This configuration is chosen when the URM block is surrounded by a steel or concrete frame along two adjacent block boundaries, as illustrated in Figure 4b. The connectivity of the block to the frame elements requires a transfer of forces and moments between the edges connected to the frame. The adoption of Hermitian polynomials allows a satisfactory representation of the separation at the physical interface between the frame components and masonry infill.

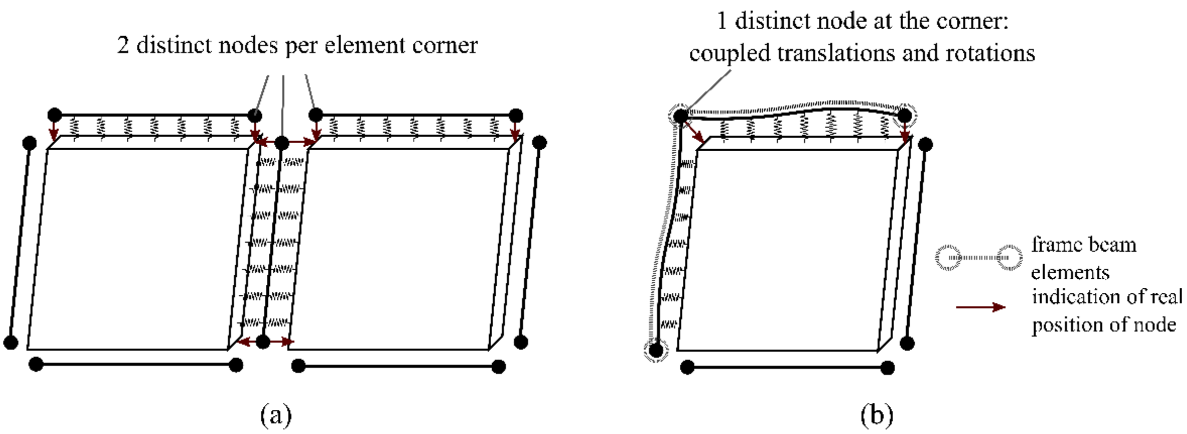

Figure 4. Types of nodal connectivity: (a) Adjacent URM blocks, (b) URM surrounded by frame

3 Macroelement formulation

In the following, the formulation of the macroelement is presented within a FEM framework. At first, the kinematics of the element in terms of basic and additional DOFs is detailed. Subsequently, the stress and strain measures of the cohesive boundaries are derived outlining the adopted constitutive relations. The behaviour of the nonlinear springs, governing the deformation modes of the inner block, and their calibration, based on specific macroscopic failure modes of a URM block, is then discussed. The derivation of the resistance force vector and the stiffness matrix of the element, on the basis of the stress and strain measures, is presented. Finally, the mass matrix defining the dynamic characteristics of the macroelement is derived.

3.1 Kinematics

As detailed in Section 2.2, each macroelement is defined through n distinct nodes ($2 \leq n \leq 8$). The element is implemented in a 3D FEM framework, where each node is characterised by 3 translational and 3 rotational degrees of freedom (DOFs). In the local element coordinate system XYZ shown in Figure 2a, the translational DOFs are noted as u_X, u_Y, u_Z and the rotational ones as θ_X, θ_Y, θ_Z. The vector of size $6n$ containing all the nodal DOFs of the macroelement in the element reference system XYZ can be expressed as:

$$\boldsymbol{U_s} = \begin{bmatrix} u_{X,1} & u_{Y,1} & u_{Z,1} & \theta_{X,1} & \theta_{Y,1} & \theta_{Z,1} & \dots & u_{X,n} & u_{Y,n} & u_{Z,n} & \theta_{X,n} & \theta_{Y,n} & \theta_{Z,n} \end{bmatrix}^T \tag{1}$$

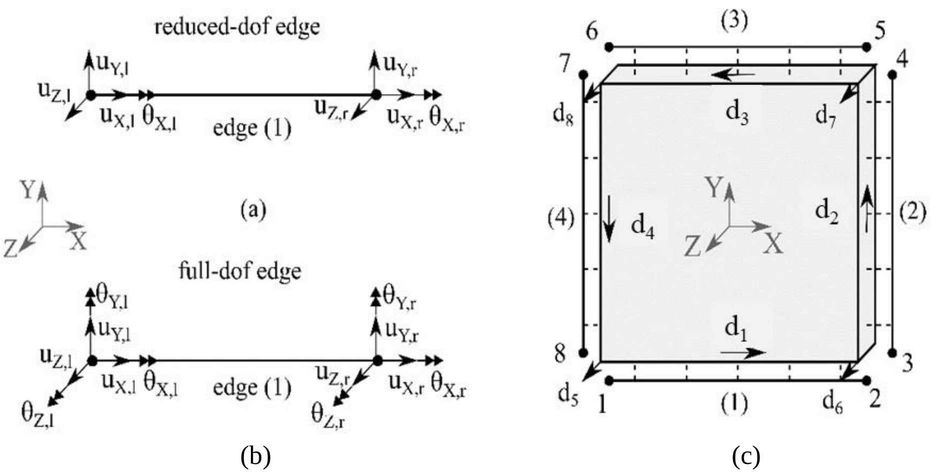

Figure 5. Schematic representation of the DOFs of the macroelement: (a-b) Basic DOFs of external edges in the local element coordinate system, (c) Inner block additional DOFs

When an external edge connects two macroelements, the interacting faces of the two adjacent blocks are plane, since the interpolation of the displacements within the inner block is linear. Therefore, a linear two-noded external edge is used to provide connectivity between adjacent macroelements. In this case, the rotational DOFs associated with bending of the edge in- and out-of-plane are not required. On the contrary, the twisting rotations are necessary to represent relative displacements at the interface under out-of-plane bending. Hence, edges connecting adjacent macroelements are defined by 4-DOF nodes, as shown in the example of Fig. 5a and are referred to as *reduced-DOF* edges. On the other hand, an external edge, connected to a beam element (e.g. representing a portion of a frame component interacting with the masonry infill), is described by 6-DOF nodes, so that it can represent a deformation mode compatible with the elastic deformation of the beam element under bending. These edges are referred to as full-DOF edges. An example is given in of Fig.5b.

In addition to the nodal DOFs, each macroelement has eight additional DOFs, illustrated in Fig.5c, which govern the deformation modes of the inner block. The additional DOFs d_1 to d_4 define the in-plane displacement of each rigid face of the block, while d_5 to d_8 define the out-of-plane displacement at each corner of the block. A linear interpolation of these displacements is assumed within the block domain. The vector of the additional DOFs of the macroelement is noted as:

$$\boldsymbol{U_a} = \begin{bmatrix} d_1 & d_2 & d_3 & d_4 & d_5 & d_6 & d_7 & d_8 \end{bmatrix} \tag{2}$$

while the vector containing all the basic and additional DOFs of the element is given by:

$$\boldsymbol{U} = \begin{bmatrix} \boldsymbol{U_s} & \boldsymbol{U_a} \end{bmatrix}^T \tag{3}$$

3.2 Cohesive boundaries

The interfaces along the four macroelement boundaries are characterised by a cohesive-frictional behaviour governed by a 3D plasticity-damage constitutive law. This law defines the relationship between the relative displacements $\boldsymbol{\varepsilon_i}$ and the interface tractions $\boldsymbol{\sigma_i}$ at each Gauss Point within the 2D domain of the zero-thickness interface, as illustrated in Fig. 6a. Both the relative displacements and the interface tractions are expressed in the local reference system xyz of boundary (i), shown in Fig. 6 where y represents the direction normal to the zero-thickness interface mid-surface and x and z represent the tangential directions:

$$\boldsymbol{\varepsilon_i} = \begin{bmatrix} \varepsilon_{x,i} & \varepsilon_{y,i} & \varepsilon_{z,i} \end{bmatrix}^T \tag{4}$$

$$\boldsymbol{\sigma_i} = \begin{bmatrix} \sigma_{x,i} & \sigma_{y,i} & \sigma_{z,i} \end{bmatrix}^T \tag{5}$$

At first, the strain measure $\boldsymbol{\varepsilon_i}$ will be defined. Let $\boldsymbol{u_{int,i}}$ be the displacement field along the face of the block constituting the internal side of the zero-thickness interface (i), $i = 1{:}\,4$, as shown in Figure 6b. The field $\boldsymbol{u_{int,i}}$ depends on the additional DOFs of the element sketched in Figure 6b. Also, let $\boldsymbol{u_{ext,i}}$ be the displacement field along the 2D surface defined by the two-noded edge (i), as shown in Figure 6b. The field $\boldsymbol{u_{ext,i}}$ can be interpolated by the nodal DOFs of the edge. Hence, the relative displacement between the two sides of the zero-thickness cohesive interface can be written as:

$$\boldsymbol{\varepsilon_i} = \boldsymbol{u_{int,i}} - \boldsymbol{u_{ext,i}} = \boldsymbol{N_{a,i}}\boldsymbol{U_a} - \boldsymbol{N_{s,i}}\boldsymbol{U_s} \qquad \textbf{(6)}$$

where $\boldsymbol{N_{a,i}}$ and $\boldsymbol{N_{s,i}}$ are the matrices which determine the interpolation of the displacement fields $\boldsymbol{u_{int,i}}$ and $\boldsymbol{u_{ext,i}}$ by the additional DOFs $\boldsymbol{U_a}$ and the basic nodal DOFs $\boldsymbol{U_s}$ of the macroelement, respectively. Details on the derivation of these matrices for reduced-DOF and full-DOF edges are provided in Appendices A and B.

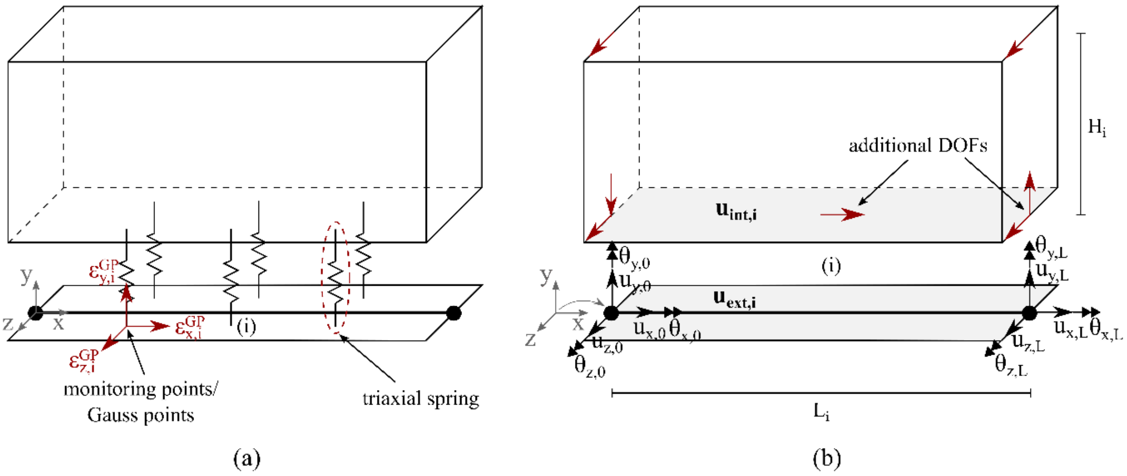

Figure 6. (a) Local reference system and monitoring points along macroelement cohesive boundary; (b) Displacement fields on the two sides of the cohesive interface

Having defined the relative displacements from the macroelement DOFs, a 3D cohesive-frictional constitutive law is employed to derive the interface tractions $\boldsymbol{\sigma_i}$ at each Gauss Point along the interface. The law employed here is based on the plasticity-damage formulation developed by Minga et al. [33]. It reproduces the main characteristics of the cyclic behaviour of cohesive-frictional interfaces: softening behaviour in tension and shear, stiffness degradation depending on the level of damage, recovering of normal stiffness in compression and residual (plastic) strains at zero stresses when the interface is damaged. Additionally, the effect of masonry crushing in compression is taken into account, through negative plastic normal strain at the interfaces of the crushed area.

The elastic yield domain is described by three surfaces in the stress domain, as shown in Fig. 7. Surface F_2 controls the shear sliding failure mode and it is based on the cohesion c and the friction angle $tan\varphi$ of the modelled URM block within the plane of the interface (which is parallel or perpendicular to the bed joints). Surface F_1 sets a tensile cap representing the flexural failure mode, which is defined by the tensile strength f_t of masonry in the direction normal to the interface. Finally, surface F_3 constitutes a compressive cap which defines the onset of masonry crushing when the normal stress exceeds the compressive strength of masonry f_c. When the yield domain is exceeded, plastic deformation and damage develop, producing a softening behaviour in the $\sigma_i - \varepsilon_i$ response in the normal and tangential directions. When the damage under tension or shear is fully developed, the normal tensile stress drops to zero, while the tangential stresses follow a Mohr-Coulomb friction law, i.e. their residual value depends on the compressive stress. On the other hand, when the compressive cap is exceeded, the negative plastic deformation and the damage under compression reproduce in a phenomenological way the crushing of masonry within the area of influence of the specific Gauss point. It is stressed that one of the most important characteristics captured with the use of the adopted damage-plasticity constitutive law is the direct coupling between the normal and tangential directions. This means that the opening of a crack (i.e. the development of damage within the interface) affects both the normal and the tangential directions, as physically expected. Furthermore, it ensures that the response under shear is directly dependent on the level of normal stresses.

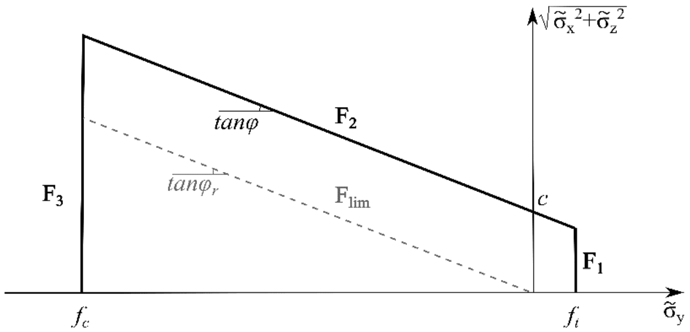

Figure 7. Multi-surface yield domain of interface constitutive law [33]

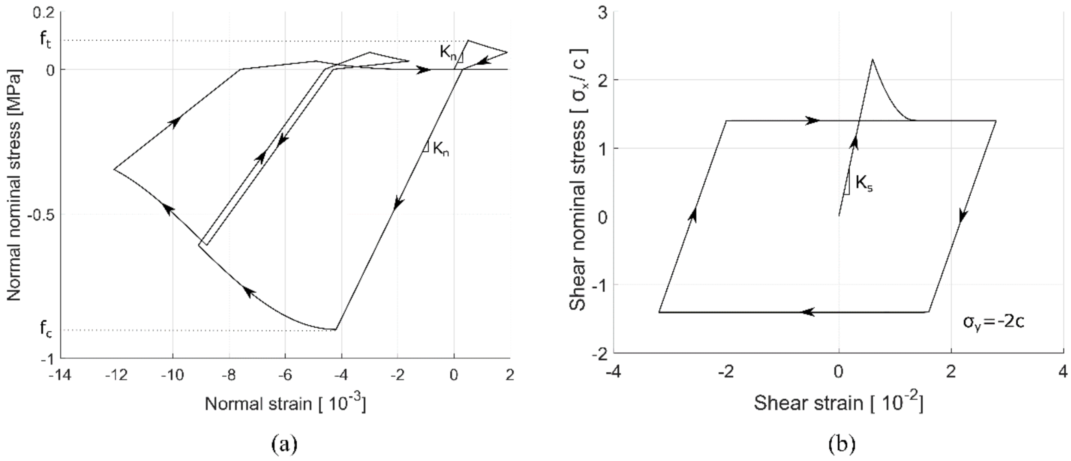

Figure 8. Illustrative examples of the cyclic constitutive law employed at the cohesive interfaces [33]: (a) normal direction; (b) tangential direction

Figure 8 shows examples of the cyclic behaviour obtained with the interface constitutive law in the normal and tangential directions. Since the elastic deformation of the URM block is concentrated in the interfaces, as outlined in Section 2.1, the elastic stiffness parameters K_n and K_s represent the elastic axial and shear stiffness of the masonry per unit length of the area of influence of the specific interface. Let E_X and E_Y be the Young's modulus of masonry in the direction of the local element axes X and Y respectively, and G be the elastic shear modulus of masonry. Then:

$$K_{n,1} = K_{n,3} = \frac{2E_Y}{H} \quad , \quad \boldsymbol{K_{n,2} = K_{n,4} = \frac{2E_X}{L}} \qquad \textbf{(7)}$$

$$K_{s,1} = K_{s,3} = \frac{2G}{H} \quad , \quad \boldsymbol{K_{s,2} = K_{s,4} = \frac{2G}{L}} \qquad \textbf{(8)}$$

where the numbers in the subscripts define the edge of the macroelement. The remaining parameters of the model have been outlined in the definition of the yield domain.

3.3 In-plane shear spring

The in-plane shear deformation is defined by a single parameter, conveniently controlled by an individual nonlinear spring. This parameter can be related to the additional in-plane DOFs of the element. In particular, the in-plane rigid body motion and the deformation of the in-plane shear spring are governed by d_1, d_2, d_3 and d_4 (Figure 5b). Considering α as the angle between the diagonal spring and the top edge of the macroelement, as shown in Fig. 9, then:

$$u_d = \boldsymbol{N_d}\,\boldsymbol{U_a} \tag{9}$$

where:

$$\boldsymbol{N_d} = [cos\alpha \quad -sin\alpha \quad cos\alpha \quad -sin\alpha \quad 0 \quad 0 \quad 0 \quad 0] \tag{10}$$

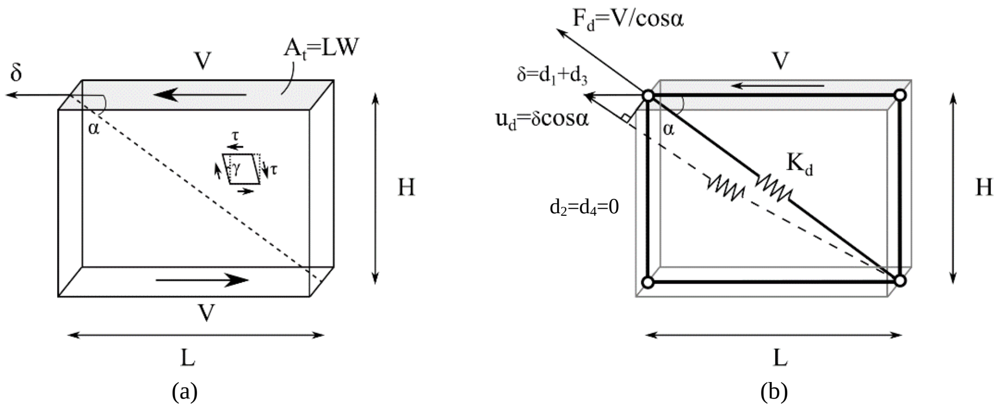

Figure 9. Calibration of in-plane shear spring: (a) homogeneous masonry plate under pure shear; (b) macroelement inner block

The force F_d developed in the spring is based on a constitutive law, which reproduces, in a phenomenological way, the global response of a masonry block that fails due to diagonal cracking under in-plane shear. The piecewise-linear law illustrated in Figure 10 is employed, as it approximately captures the main characteristics of the specific cracking pattern, discussed for example in [34].

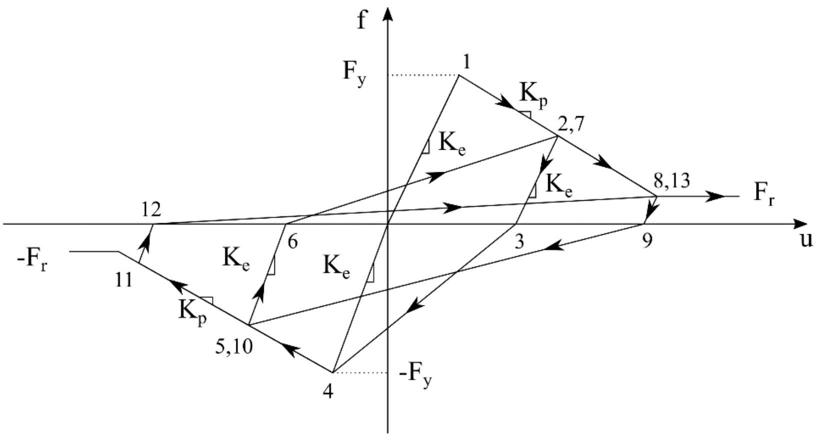

Figure 10. Constitutive law employed for the macroelement springs

The model parameters for the diagonal shear spring, noted as F_y^d, F_r^d, K_e^d, K_p^d, can be estimated as functions of the macroscopic masonry properties by considering the equivalence of the macroelement inner block to a homogeneous masonry plate under pure shear Fig. 9a. More specifically, the elastic stiffness K_e^d and the post-peak stiffness K_p^d can be calculated form the masonry elastic and post-peak shear moduli G_e and G_p, which can be obtained from physical experiments, using the relationships:

$$K_e^d = G_e \frac{LW}{Hcos^2 a} \quad , \quad K_p^d = G_p \frac{LW}{Hcos^2 a} \tag{11}$$

where L, H and W represent the length, height and thickness of homogeneous masonry plate.

The shear strength of the diagonal spring F_y^d can be determined employing existing strength prediction models which allow for unit interlocking and the cohesive and frictional nature of the masonry response in shear. In this work, F_y^d is calculated based on the macroscopic masonry shear strength provided by the Mann and Muller model [35] using the relationships:

$$F_y^d = \tau_{Y,0} + \mu_d \sigma_n \frac{LW}{Hcosa} \tag{12}$$

$$\mu_d = \frac{\mu'}{1 + 2\mu' \frac{\Delta_H}{\Delta_L}} \tag{13}$$

$$\tau_{Y,0} = \frac{c'}{1 + 2\mu' \frac{\Delta_H}{\Delta_L}} \tag{14}$$

where $\tau_{Y,0}$ is the shear strength at zero confinement, μ_d a parameter which defines the influence of the confinement to the shear strength, c' and μ' are the cohesion and friction angle of the masonry joints, while Δ_H and Δ_L are the length and height of the brick unit respectively. Finally, σ_n is the mean normal stress applied to the URM block, which is obtained by the normal tractions at the interfaces along the boundaries at the previous converged step of the analysis.

Obviously, the ability of the diagonal spring to represent actual diagonal cracking depends on the accuracy of the adopted phenomenological macroscopic strength model. Recent research [36] pointed out that the Mann and Muller model generally provides realistic shear strength predictions for running bond brick/block-masonry, but it generally overestimates the influence of unit interlocking potentially leading to incaccurate results when used to analyse masonry components with complex bond. An alternative approach to determine the elastic and strength material parameters of the diagonal spring representing in-plane shear failure could be based on computational strategies linking the macroscale to the mesoscale [16, 18] where masonry texture is explicitly represented.

3.4 Out-of-plane diagonal bending spring

The diagonal bending behaviour of the internal block, contributing to simulate the out-of-plane response of a masonry wall, is governed by the additional DOFs d_5, d_6, d_7 and d_8. The out-of-plane diagonal bending response along a specific diagonal, Fig. 2c, can be related to a single nonlinear spring denoted as bending spring. The deformation of the out-of-plane bending spring coincides with the lateral distance between the central points of the two diagonals of the inner block mid-surface. Initially, its length is zero. In a deformed configuration, the out-of-plane bending deformation of the spring is obtained as a function of the additional DOFs d_5, d_6, d_7 and d_8:

$$u_{out} = \boldsymbol{N_{out}}\, \boldsymbol{U_a} \tag{15}$$

where:

$$\boldsymbol{N_{out}} = \frac{1}{2}[0 \quad 0 \quad 0 \quad 0 \quad -1 \quad 1 \quad -1 \quad 1] \tag{16}$$

corresponding to a bending along the diagonal 2-6.

The force F_{out} developed in the spring is obtained based on the same constitutive law employed for the diagonal spring, as outlined in Section 3.3. The constitutive behaviour of this spring is conceived to reproduce phenomenologically the out-of-plane failure mode due to diagonal bending. In this case, there are no established simple direct mechanical models providing a macroscale description for the failure mode with diagonal cracking under out-of-plane two-way bending which can be used to determine the material parameters for the out-of-plane diagonal spring. Furthermore, a model calibration based on the results from physical tests, as the tests on solid walls in [40], would be impractical due to the complexity and the relatively high cost associated with this type of physical experiments on masonry components. Hence, a calibration of the stiffness and strength parameters (F_y^{out}, F_r^{out}, K_e^{out}, K_p^{out}) based on the results of detailed mesoscale models is proposed here. The use of more general multiscale strategies employing homogenisation principles [17] or inverse analysis [18] is expected to lead to more accurate calibration and will be considered in future research. It is worth noting that the complexity of the calibration procedure does not hinder the efficiency of the proposed modelling strategy with macroelements as it conducted off-line, considering virtual numerical experiments simulated by mesoscale models which explicitly allow for masonry bond and require simpler material calibration based on component tests on units and mortar joints.

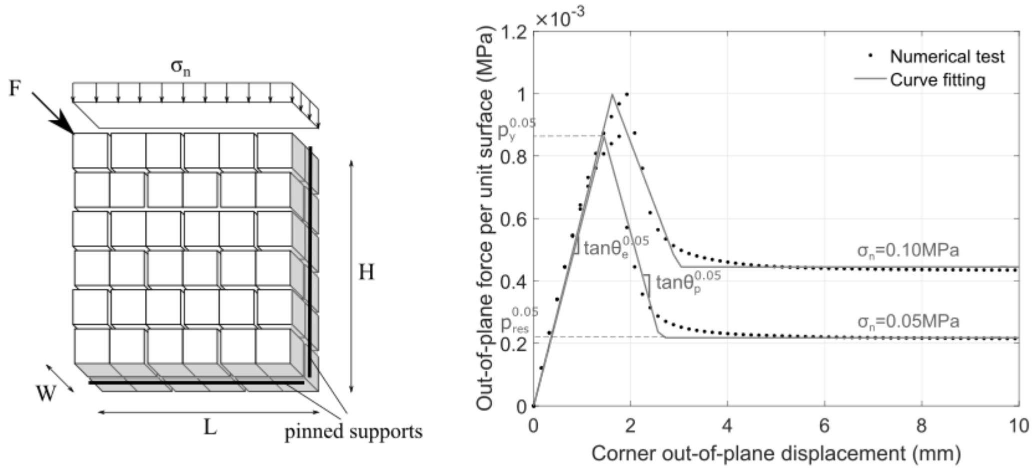

(a) (b)

Figure 11. Calibration of out-of-plane spring: (a) boundary conditions of numerical test; (b) curve fitting and parameter identification.

Thus, according to the calibration approach used in this research, numerical tests on URM blocks under out-of-plane diagonal bending modelled using the detailed 3D mesoscale approach developed by Macorini and Izzuddin [3] and enhanced in [33] are employed. A mesoscale model of a URM block with the geometric characteristics of the macroelement and a realistic representation of the bonding pattern of the examined structure is developed, as shown in the example of Figure 11a. The mesoscale block is subjected to an out-of-plane deformation mode corresponding to the out-of-plane spring activation, under different levels of normal compressive stress. An illustrative example of the nonlinear response obtained by the numerical test is shown in Figure 11b. Each experimental curve is used to calibrate a piecewise linear envelope with the form of the constitutive model of Figure 10. The parameters obtained by the curve fitting are the slope of the pre-peak (elastic) branch $tan\theta_e$, the slope of the post-peak branch $tan\theta_p$, the yield pressure per unit surface p_y, the residual pressure per unit surface p_r. The first two parameters are used for the calibration of K_e^{out} and K_p^{out} which are taken as the average of the values obtained for different levels of compressive stress:

$$K_e^{out} = \frac{1}{n}\sum_{k=1}^{n} 4LHtan\theta_{e,k} \tag{17}$$

$$K_p^{out} = \frac{1}{n}\sum_{k=1}^{n} 4LHtan\theta_{p,k} \tag{18}$$

Based on the definition of the out-of-plane spring deformation and reaction force, the out-of-plane pressure p relates to the spring reaction force F^{out} in the following way:

$$F^{out} = 2LHp \tag{19}$$

Based on Equation (20), the values of p_y and p_r obtained by the numerical tests can be transformed into spring force measures. Thus, two series of data points (σ_n, F_y^{out}) and (σ_n, F_r^{out}) are obtained. Those data points are used for the identification though linear regression of two functions which provide the parameters F_y^{out}, F_r^{out} of the spring constitutive law for different levels of applied normal stress:

$$F_y^{out}(\sigma_n) = F_{y,0}^{out} + \mu_{out,y}\,\sigma_n \tag{20}$$

$$F_r^{out}(\sigma_n) = F_{r,0}^{out} + \mu_{out,r}\,\sigma_n \tag{21}$$

Similar to the case of the shear spring, the normal stress in Equations (20) and (21) are obtained by the normal tractions at the interfaces along the boundaries at the previous converged step of the analysis.

3.5 Resistance forces and tangent stiffness of macroelement

In this section, the derivation of the macroelement resistance forces and tangent stiffness matrix in the FEM framework is outlined. The tangent stiffness of the constitutive relation between the relative displacements and the interface tractions along the boundaries is given by the relation:

$$\boldsymbol{K_i} = \frac{\boldsymbol{d\sigma_i}}{\boldsymbol{d\varepsilon_i}} \tag{22}$$

where:

$$\boldsymbol{d\varepsilon_i} = \boldsymbol{N_{a,i} dU_a} - \boldsymbol{N_{s,i} dU_s} \tag{23}$$

and the interface traction $\boldsymbol{d\sigma_i}$ increment is obtained by the cohesive frictional constitutive law described in Section 3.2. Similarly, the tangent stiffness of the constitutive relation between the deformation and reaction force of the diagonal shear spring and the out-of-plane spring is given respectively by:

$$K_d = \frac{dF_d}{du_d} \tag{24}$$

$$K_{out} = \frac{dF_{out}}{du_{out}} \tag{25}$$

where:

$$du_d = \boldsymbol{N_d}\,\boldsymbol{dU_a} \tag{26}$$

$$du_{out} = \boldsymbol{N_{out}}\,\boldsymbol{dU_a} \tag{27}$$

and the reaction forces F_d and F_{out} are obtained by the constitutive law described in Sections 3.3 and 3.4.

Let W_{int} be the virtual work of the internal forces of the macroelement and W_{ext} the virtual work of the external forces applied to the macroelement. The two quantities are obtained by:

$$W_{int} = \sum_{i=1}^{4} \int_{S_i} \boldsymbol{d\varepsilon_i^T}\,\boldsymbol{\sigma_i}\,dS_i + du_d\,F_d + du_{out}\,F_{out} \tag{28}$$

$$W_{ext} = dU^T\,F_{ext} \tag{29}$$

where S_i, $(i = 1{:}4)$ is the surface of interface i between the block and the external edge i. Taking into account Equations (23), (26) and (27), the internal work can be written as:

$$W_{int} = \boldsymbol{dU^T} \sum_{i=1}^{4} \int_{S_i} \boldsymbol{N_{s,i}^T}\,\boldsymbol{\sigma_i}\,dS_i + \boldsymbol{dU^T}\,\boldsymbol{N_d^T}\,F_d + \boldsymbol{dU^T}\,\boldsymbol{N_{out}^T}\,F_{out} \tag{30}$$

Imposing that the virtual work of the internal forces is equal to the virtual work of the external forces $\forall \boldsymbol{dU}$, we obtain the following equation:

$$\boldsymbol{dU^T}\left(\sum_{i=1}^{4}\int_{S_i} \boldsymbol{N}_{\boldsymbol{s,i}}^T\,\boldsymbol{\sigma_i}\,dS_i + \boldsymbol{N}_{\boldsymbol{d}}^T\,F_d + \boldsymbol{N}_{\boldsymbol{out}}^T\,F_{out}\right) = \boldsymbol{dU^T F_{ext}} \tag{31}$$

The resistance force vector is therefore obtained as:

$$\boldsymbol{F}^{(\boldsymbol{e})} = \boldsymbol{F_{ext}} = \sum_{i=1}^{4}\int_{S_i} \boldsymbol{N}_{\boldsymbol{s,i}}^T\,\boldsymbol{\sigma_i}\,dS_i + \boldsymbol{N}_{\boldsymbol{d}}^T\,F_d + \boldsymbol{N}_{\boldsymbol{out}}^T\,F_{out} \tag{32}$$

By differentiating the internal force vector with respect to the vector of the element degrees of freedom, the tangent stiffness matrix is obtained:

$$\boldsymbol{K}^{(\boldsymbol{e})} = \frac{\boldsymbol{dF}^{(\boldsymbol{e})}}{\boldsymbol{dU}} = \sum_{i=1}^{4}\int_{S_i} \boldsymbol{N}_{\boldsymbol{s,i}}^T\,\boldsymbol{K}_{\boldsymbol{i}}^T\boldsymbol{N}_{\boldsymbol{s,i}}\,dS_i + \boldsymbol{N}_{\boldsymbol{d}}^T\,F_d\boldsymbol{N_d} + \boldsymbol{N}_{\boldsymbol{out}}^T\,F_{out}\boldsymbol{N_{out}} \tag{33}$$

The first integral term in Eq. (33) is calculated using Gauss quadrature:

$$\begin{aligned}&\sum_{i=1}^{4}\int_{S_i} \boldsymbol{N}_{\boldsymbol{s,i}}^T\,\boldsymbol{K}_{\boldsymbol{i}}^T\boldsymbol{N}_{\boldsymbol{s,i}}\,dxdz = \sum_{i=1}^{4} \boldsymbol{N}_{\boldsymbol{s,i}}^T\,\boldsymbol{K}_{\boldsymbol{i}}^T\boldsymbol{N}_{\boldsymbol{s,i}}\,J_i\,d\xi\delta\eta\\ &= \sum_{i=1}^{4}\sum_{GP=1}^{n_{GP}} \boldsymbol{N}_{\boldsymbol{s,i}}^T(\xi_{GP},\eta_{GP})\boldsymbol{K}_{\boldsymbol{i}}^T(\xi_{GP},\eta_{GP})\,\boldsymbol{N}_{\boldsymbol{s,i}}(\xi_{GP},\eta_{GP})\,w_{GP}\,J_i\end{aligned} \tag{34}$$

where J_i is the Jacobian for the transformation between the local reference system of edge (i) and the natural reference system of the interface (i).

3.6 Mass distribution

In the case of dynamic analysis, the mass associated with each element has to be considered for the calculation of the inertia force and potentially the mass proportional damping force. For simplicity, the mass of the element is associated with the translational nodal degrees of freedom of the external edges. Let ρ be the density of masonry. Then the total mass of the element is given by the equation:

$$m_e = \rho LHW \tag{35}$$

Since the mass is distributed along the element edges, let ρ_s denote the mass per unit length of the external edges:

$$\rho_s = \frac{m_e}{2L + 2H} \tag{36}$$

The mass matrix of the element is given by the following expression:

$$\boldsymbol{M} = \rho_s \sum_{i=1}^{4}\int_{\Omega_{s,i}} N_{s,i}^T\,N_{s,i}\,d\Omega_s \tag{37}$$

4 Numerical examples

In this section, the modelling approach with masonry macroelements is used for the analysis of URM structures under in-plane and out-of-plane loading. Each case examines the ability of the macroelement to reproduce the behaviour of masonry structural components and systems under different boundary and loading conditions. To assess the capacity of the macro-models to predict the response of masonry structures with accuracy, the numerical predictions are compared against experimental results found in the literature. All the analyses have been performed using ADAPTIC [37].

4.1 Modal analysis of URM components

The representation of the linear dynamic characteristics of a URM component by a macroelement description is examined herein. For this, the results of the eigenvalue analysis of a mesoscale model of a URM wall are compared to the corresponding results obtained by two different macroelement representations of the same wall. The mesoscale model – based on the work in [10] – is considered as the reference model that provides an accurate representation of the panel characteristics. The comparison aims to investigate the accuracy in the linear domain both in terms of stiffness and mass property representation. A single-wythe running bond URM wall, with length and height of 1000×1350 mm^2 and thickness of 110 mm, is modelled. The wall is fully restrained at the bottom side. For the mesoscale description, the material characteristics reported in Table 1 are adopted. Two macroelement models have been developed: model 1 with a 3×3 mesh and model 2 with a 4×4 mesh. The macroscopic material characteristics for the macroelement models, equivalent to the mesoscale material properties, are reported in Table 2. Those values have been derived based on elastic analyses of the mesoscale model under the respective deformation modes.

Table 1: Elastic material parameters for mesoscale model

Mortar joints		Bricks	
Normal stiffness K_n [N/mm^3]	48	**Young's modulus E_b [N/mm^2]**	800
Tangential stiffness K_t [N/mm^3]	21		

Table 2: Elastic macroelement material parameters

Young's modulus E_Y [N/mm^2]	Young's modulus E_X [N/mm^2]	Shear modulus G_e [N/mm^2]	Out-of-plane elastic stiffness E_{out} [N/mm]
2700	4000	478	2690

Eigenvalue analysis is performed in the mesoscale and macroelement models of the wall. The modal shapes corresponding to the first four modes obtained with the mesoscale model are shown in Figure 12a, while Figure 12b shows the respective modal shapes of the macroelement model 1. It is noted that the modal shapes of macroelement model 2 are practically coincident, so they are not plotted for conciseness. The modal periods of each model corresponding to the first seven modes are shown in Figure 13. The sum of the mass participation factor of the first seven modes is 63-85% along all three axes. It can be observed that the modal shapes obtained by the mesoscale and macroscale representations are equivalent, which indicates that the initial stiffness and the mass matrix defined in the macroelement provide a very accurate approximation of the stiffness and the mass distribution in the component. Furthermore, the modal periods of the macroelement models are close to the reference periods obtained by the mesoscale representation. The discrepancy for model 1 is ranging between 2.1% and 21.2%, with the exception of mode 6, where the difference reaches 35%. The accuracy of model 2 is even higher, with the discrepancy ranging from 0.4% in the first modal period to 11.9% in the period of the fourth mode corresponding to the in-plane deformation.

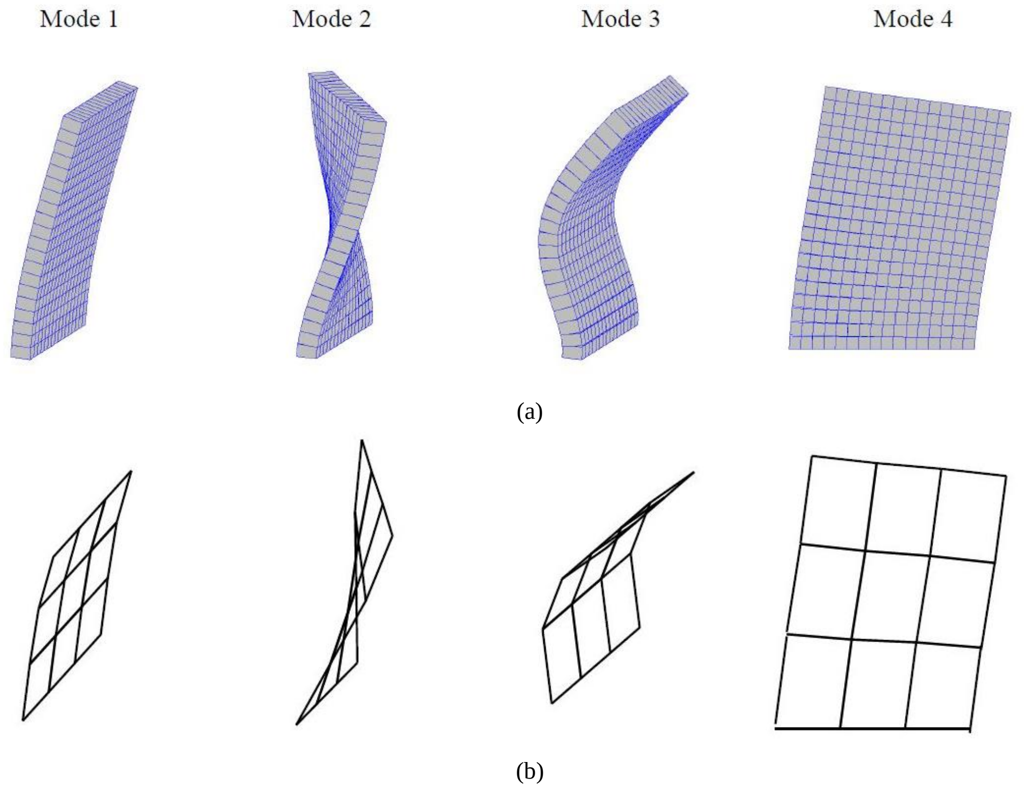

Figure 12. Modal shapes for the four first modes obtained with (a) the mesoscale model and (b) the macroelement model 1

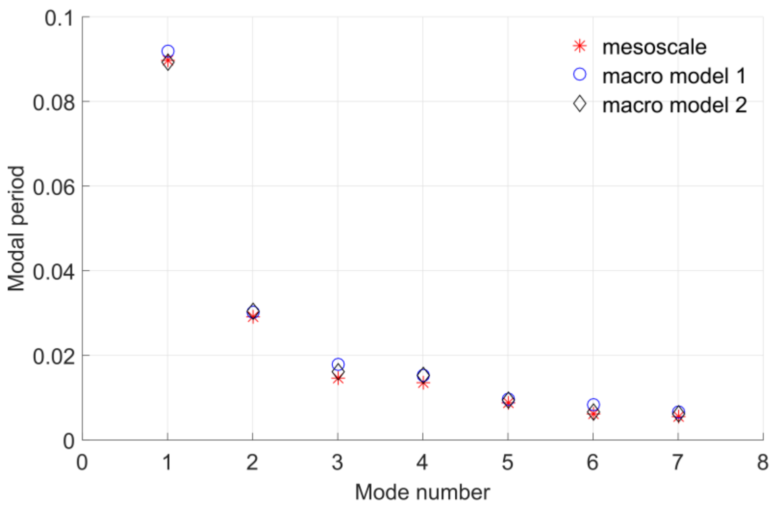

Figure 13. Modal periods of the URM wall obtained with the mesoscale and the macroscale representations

4.2 In-plane response of masonry piers

The second numerical example presented herein concerns the in-plane response up to collapse of masonry piers, which constitute critical components of perforated walls in URM buildings subjected to substantial in-plane shear forces and bending moments when these structures resist earthquake loading. For this, the experiments performed by Anthoine et al. [38] are simulated. Two URM wall specimens, the *short wall* with aspect ratio of 1.35 and the *tall wall* with aspect ratio of 2.0, were tested under in-plane shear loading. The tested wall specimens were connected to a rigid base through a mortar bed joint. A stiff beam, which was forced to remain horizontal, transferred uniform compressive stress of 0.6 MPa to each wall. Horizontal displacement cycles of increasing magnitude were imposed to the top beam. Each specimen developed a distinct failure mechanism, associated with dissimilar characteristics of the cyclic response curve. The *short wall* specimen developed diagonal shear cracking and failure, while the *tall wall* specimen developed horizontal cracking due to flexural bending and rocking cyclic behaviour, without strength degradation. The ability of the proposed macroelement modelling approach to predict the main monotonic and cyclic response characteristics of the two piers and their distinct failure modes is investigated in the following.

Table 3. Material parameters for macroelement cohesive interfaces used in masonry pier models

	Young's modulus E **[N/mm²]**	**Tensile strength** f_t **[N/mm²]**	**Cohesion** c **[N/mm²]**	**Friction angle** $\tan\phi$	**Fracture energy** G_f **[N/mm]**	
					Mode I	Mode II
Horizontal	2500	0.1	0.23	0.58	0.05	0.10
Vertical	1500	0.68	1.56	0.8	0.05	0.10

Table 4. Material parameters for macroelement diagonal shear spring used in masonry pier models

Elastic shear modulus G_e **[N/mm²]**	**Post-peak shear modulus** G_p **[N/mm²]**	**Shear strength at zero confinement** $\tau_{Y,0}$ **[N/mm²]**	**Coefficient of friction** μ_d
580	-200	0.17	0.43

The two specimens are modelled with the proposed approach with reduced-DOF edges (allowing connectivity between URM blocks), using two alternative meshes with 2×2 (mesh 1) and 3×3 (mesh 2) macroelements. In all the models, the element edges along the bottom are fully restrained, simulating a rigid boundary. The bottom interfaces corresponding to the restrained edges represent the frictional surface between the wall specimens and the rigid base. The edges along the top of the walls are forced to remain horizontal by coupling the translations of their nodes along the Y direction. Horizontal displacement cycles along the X direction are applied to the same nodes. Since all loads are applied in-plane and the top edges have common X and Y displacements, they remain rigid and horizontal, thus simulating the slab support. The interfaces corresponding to the top edges represent the frictional surface between the wall and the steel beam. The compressive stress σ_n=0.6 MPa is applied through nodal forces at the top edges. The material properties used in the analysis are given in Table 3 and Table 4. The Young's modulus of masonry adopted for the horizontal interfaces in the vertical direction E_Y is consistent with the results from the physical tests on the materials used for the construction of the specimens as reported in [34]. The Young's modulus in the horizontal direction for the vertical interfaces is taken as E_X=0.6E_Y. The remaining parameters for the horizontal interfaces are the material properties of the wall bed joints, taken from previous works that presented mesoscale simulations of the same experiments [33]. On the other hand, the vertical interfaces of the macroelement refer to a boundary comprised of both head joints and through-brick potential crack paths. Therefore, their parameters are estimated as the average values of the properties of head joints and brick cracking surfaces, also taken from mesoscale numerical representations. Along all boundaries, the value of the compressive strength of masonry is f_c = 6.2MPa [34] and the dilation angle is assumed as zero. Regarding the shear spring, the macroscopic shear parameters are based on the values suggested by Magenes and Fontana [24].

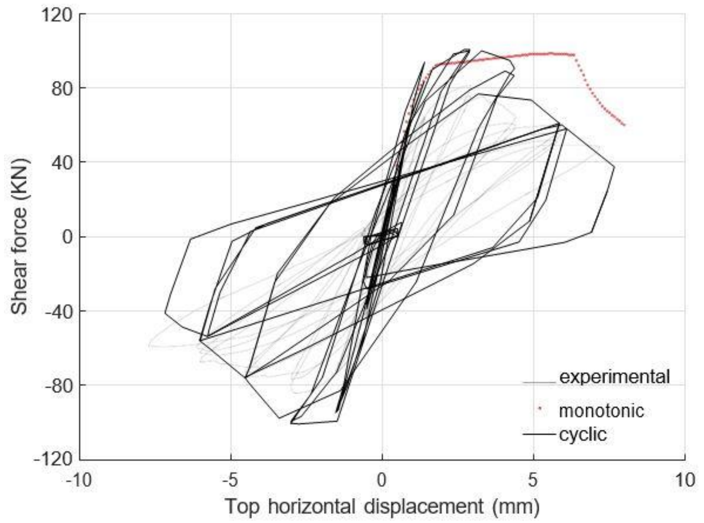

(a)

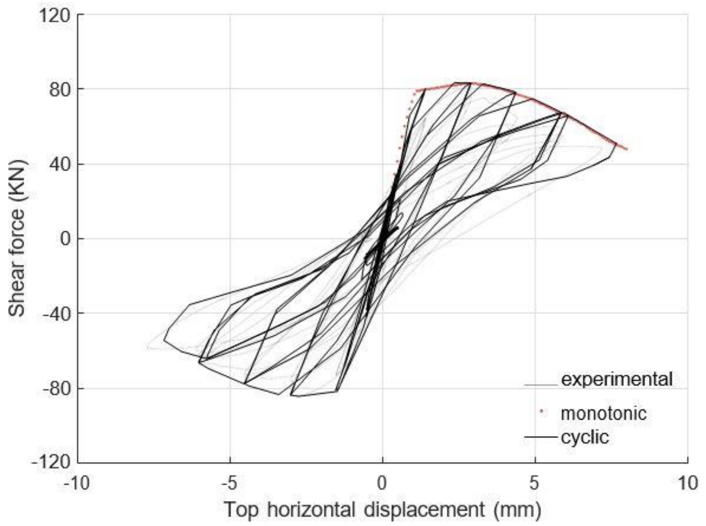

(b)

Figure 14. Numerical-experimental comparison of the force-displacement response for *short wall* under in-plane monotonic and cyclic loading: (a) mesh 1; (b) mesh 2

In Figure 14, the experimental curve for the short wall specimen, showing the variation of the shear force against the horizontal top displacement, is compared against the numerical results obtained with the two macroelement models under monotonic and cyclic loadings. The numerical curve for mesh 2 is in very close agreement with the experimental results. The maximum shear capacity of the wall and the corresponding drift are accurately captured. Furthermore, the rate of strength and stiffness degradation are reproduced in a very accurate way and, consequently, the amount of hysteretic energy dissipation at each cycle is close to the experimental observations. On the other hand, the use of the coarser mesh 1 leads to an overestimation of the force and hysteretic energy dissipation capacities and the strength degradation that is more abrupt than the one predicted with mesh 2. The relatively large discrepancy between the results obtained using different mesh characteristics can be explained by closely observing the deformed shapes at maximum displacements in Figure 15a and the damage in the diagonal shear springs in Figure 15b, and comparing them with the experimental cracking pattern in Figure 15c. In the experiment, the wall developed diagonal cracks close to the corners, that meet in a vertical cracking zone at the centre of the specimen (Figure 15c). In the 4-element model (mesh 1), the sensitive central zone is not represented independently from the corner zones. As a result, all elements deform almost uniformly until the yield point of the shear springs, which results in the overestimation of the capacity. Furthermore, after the yield point, the two elements of the top row develop abrupt softening - as can be derived by the advanced damage state at the end of the analysis shown in Figure 15b - producing the practically linear post-peak behaviour. On the contrary, in the 9-element model (mesh 2) the 3 macroelements at mid-length represent the central zone of the wall,where shear cracking initiates and develops, as can be observed in the deformed shape in Figure 15a. In addition, the four corner macroelements correspond to the zones of diagonal cracking. Indeed, Figure 15b shows significant shear damage in the diagonal shear springs of three central and two bottom corner macroelements, but shear damage in the two top corner macroelements is underpredicted. Overall, this level of mesh refinement achieves an adequate representation of the analysed URM component that ensures accurate prediction of the cyclic response (Figure 14b). It is noted that a 4×4-element model has also been tested and the resulting cyclic response is practically coincident with the one obtained using the 9-element model, as expected for any mesh with a larger number of macroelements than 3×3 [39].

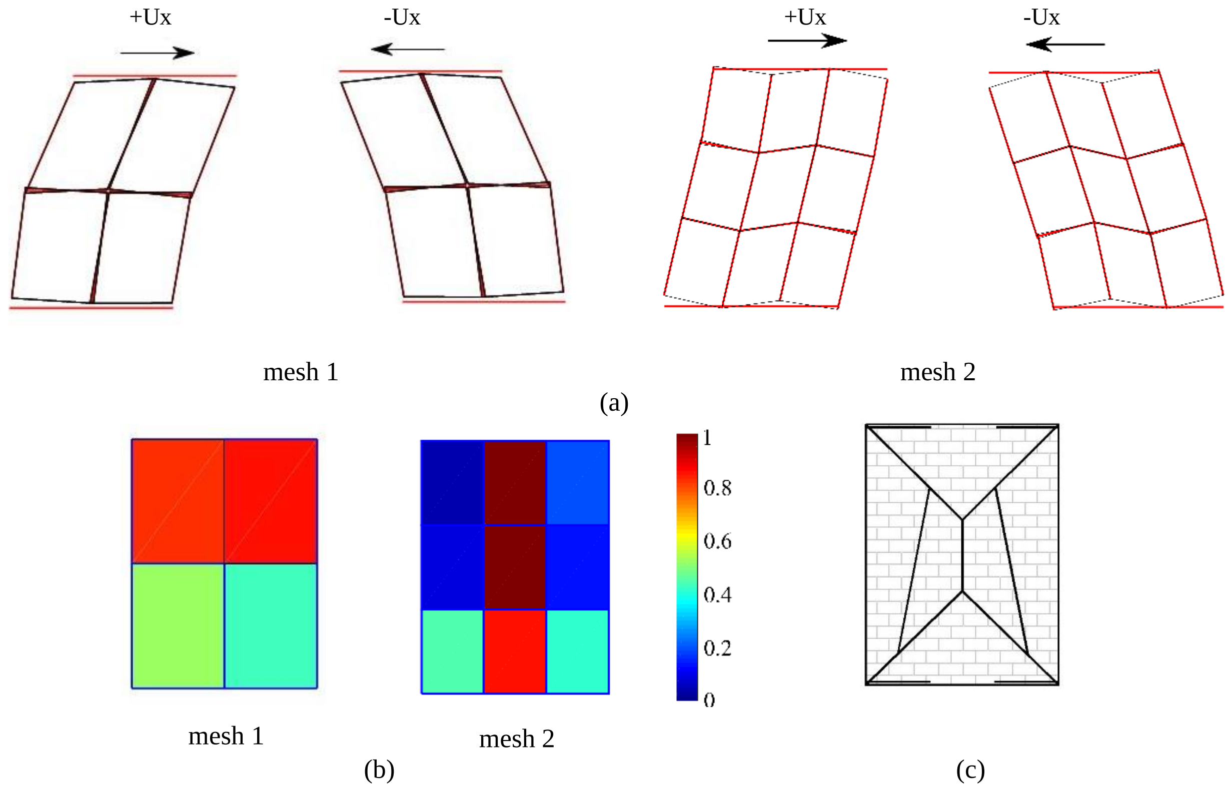

Figure 15. *Short wall* under cyclic loading: (a) deformed shape at edges of largest cycle for meshes 1 and 2; (b) strength degradation of diagonal shear springs at the end of the analysis for meshes 1 and 2; (c) experimental cracking pattern [37]

Fig. 16 shows the numerical-experimental comparisons of the global response of the *tall wall*. Also in this case, two models with 2×2 (mesh 1) and 3×3 (mesh 2) macroelements are employed in the numerical simulations. Both models provide a good representation of the pure rocking behaviour, which characterises the physical response of the *tall wall* specimen. The envelope of the cyclic behaviour is effectively captured, meaning that the capacity of the wall in the case of flexural failure is accurately predicted also by the model with the coarser mesh. Furthermore, as it can be observed from the deformed shapes plotted in Fig. 17a, flexural cracking appears at the top and bottom interfaces, while the diagonal springs in this case remain elastic. This provides a good representation of the experimental cracking pattern (Fig. 17b) which confirms the ability of the macro-element description with a correct calibration of the material parameters to reproduce the influence of the wall geometry and the actual failure mode for different wall aspect ratios. However, the cyclic response prediction does not capture the increase in the amount of energy dissipation as the drift increases which is observed in the experimental tests. This could be partly due to the assumption of elastic unloading-reloading in the employed constitutive model [33], which is a simplification of the real unloading-reloading path that might involve a certain level of hysteresis. Additionally, it can be partially explained by the "perfect" symmetrical rocking behaviour produced in the numerical simulations, which cannot appear in an experimental test of a real brick wall, where various effects, such as non-uniform properties of the joints and lack of perfect symmetry, might play a significant role.

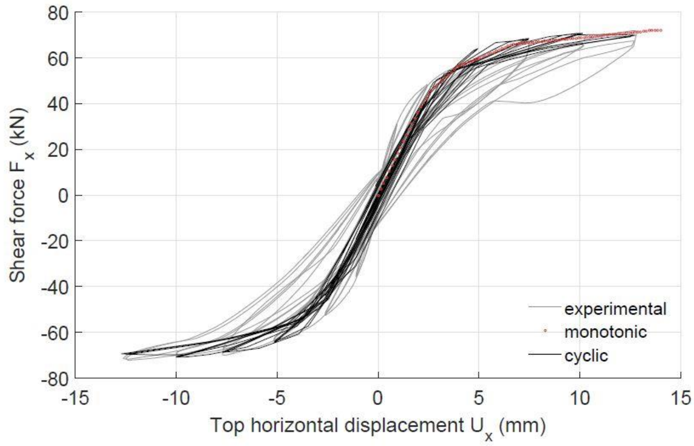

(a)

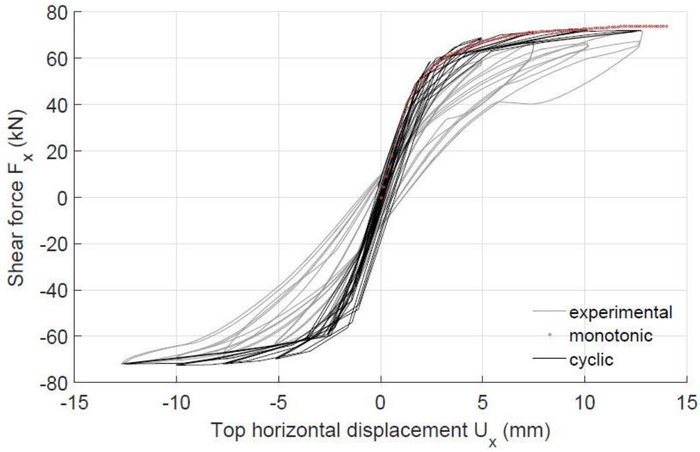

(b)

Figure 16: Numerical-experimental comparison of the force-displacement response for *tall wall* under in-plane monotonic and cyclic loading: (a) mesh 1; (b) mesh 2

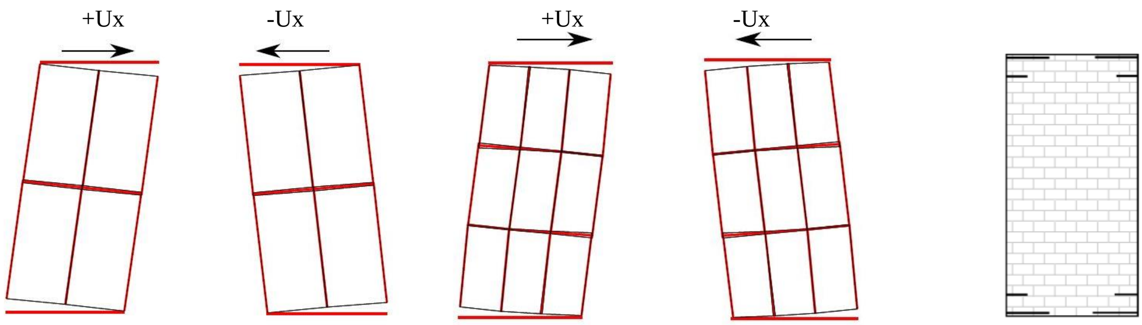

mesh 1 mesh 2 (b)

(a)

Figure 17. *Tall wall* under cyclic loading: (a) deformed shape at edges of largest cycle for meshes 1 and 2; (b) experimental cracking pattern [38]

4.3 *Two-way bending of URM walls*

The developed macroscale description has been used also to investigate two-way bending of URM components. This mode appears when out-of-plane loads are applied to a wall that is connected along the vertical edges to return walls. It is a common configuration in old URM buildings, where the out-of-plane actions often cause severe damage. To investigate the ability of the macroelement representation to accurately predict this type of response, the experimental tests performed by Griffith et al. [40] are simulated. In particular, the solid wall specimens 1 and 2 and the specimens with window openings 3 and 5 of the experimental program are modelled herein. The analysed specimens consist of a main wall of 4000×2500 mm^2 and 480 mm long return walls on both sides. Specimens 3 and 5 contain an opening in the main wall, as shown in Figure 18. The walls were built with running bond pattern, overlapping at the intersections between perpendicular panels. The main wall was simply supported along the top and the bottom edge in the direction of the loading and restraints were imposed along the vertical edges of the return walls to achieve a full moment connection. Uniform pressure was applied at the two faces of the main wall resulting in cyclic out-of-plane response. In specimens 1 and 3, a uniform compressive stress of 0.1 MPa was applied at the top to examine the influence of confinement.

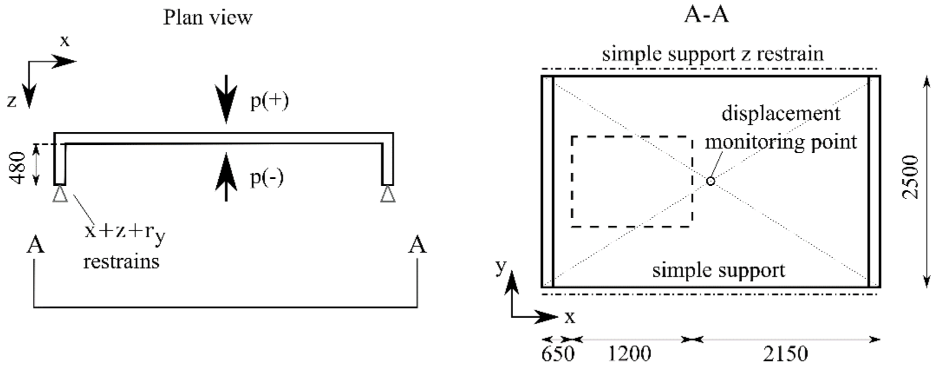

Figure 18. Geometry and boundary conditions of the experimental specimen with window opening under two-way bending

The solid wall specimens are modelled with a mesh of 8×4 macroelements, with the main wall represented by 6×4 macroelements of equal size and each lateral wall represented by 1×4 equal sized elements. For specimens 3 and 5, a mesh of macroelements is employed for the main wall to accommodate the opening, while the lateral walls are represented by 1×6 macroelements. All elements have reduced-DOF edges. The external edges along the bottom surface of the model are fully restrained. The top edges of the main wall are restrained only in the out-of-plane direction, creating pinned supports. The vertical edges of the return walls are restrained in the direction of the X and Z axis and are not allowed to rotate around the vertical Y axis. Nodal forces are applied to the top edges representing the compressive stress, where necessary. The uniform lateral pressure along the surface of the main wall is applied through nodal forces with values that correspond to the area of influence of each node.

Table 5. Material parameters for macroelement cohesive interfaces used in models for walls under two-way bending

	Young's modulus E [N/mm^2]	**Tensile strength f_t [N/mm^2]**	**Cohesion c [N/mm^2]**	**Friction angle tan ϕ**	**Fracture energy G_f [N/mm]**	
					Mode I	Mode II
Horizontal	3540	0.163	0.75	0.24	0.05	0.10
Vertical	2124	1.08	2.43	0.56	0.05	0.10

The material parameters for the horizontal and vertical interfaces are reported in Table 5 and are derived by the properties of the interfaces in the mesoscale description [33] as discussed in Section 3.2. The parameters of the out-of-plane springs are calibrated based on the procedure summarised in Section 3.4. Details on the calibration are provided in [39].

At first, monotonic surface loading was applied to the four models to investigate the influence of the opening and the level of compressive stress in the wall initial capacity and ductility. The numerical monotonic response of the solid wall models is presented in Figure 19, where the out-of-plane displacement at the monitoring point is plotted against the applied pressure for different levels of compressive stress. The numerical curves are compared to the envelope of the experimental response [40]. It can be observed that the macroelement models provide an accurate prediction of the out-of-plane capacity of the walls, also accounting for the influence of compressive stresses. Additionally, the post-peak softening rate and the strength at the maximum displacement attained are approximately captured. The increased rate of strength degradation in the case of σ_n=0.1MPa, could be more accurately reproduced if the influence of the compressive stresses to the post-peak slope of the out-of-plane spring was taken into account. The latter characteristic will be re-examined in future work.

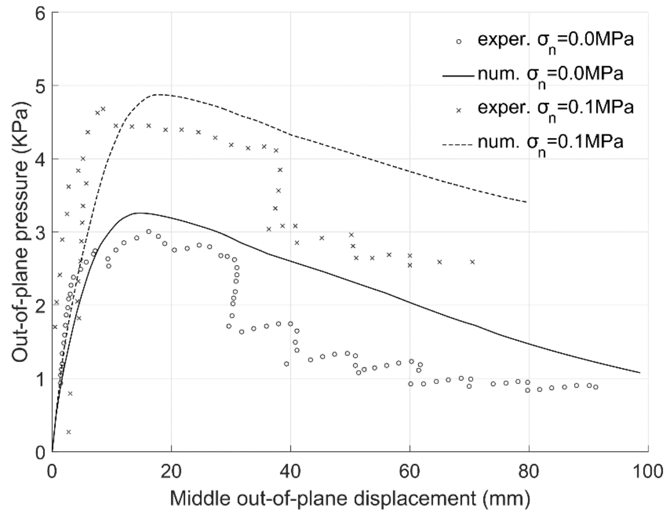

Figure 19. Numerical monotonic response of solid wall specimens under out-of-plane loading compared to envelope of experimental response for different levels of compressive stress

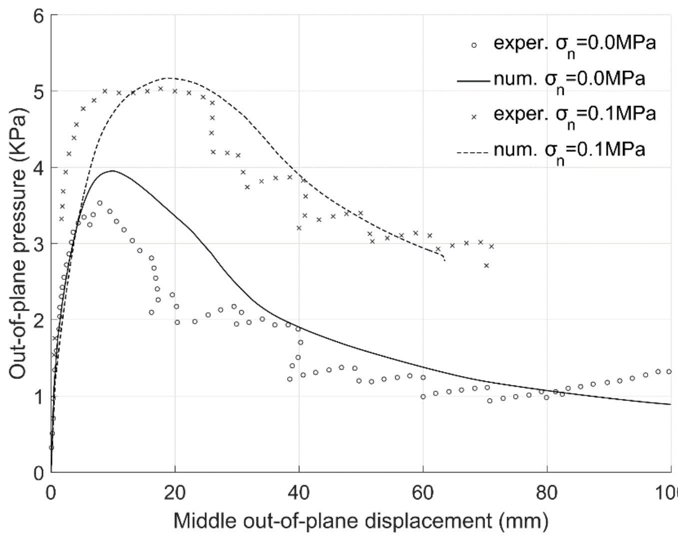

Figure 20. Numerical monotonic response of window wall specimens under out-of-plane loading compared to envelope of experimental response for different levels of compressive stress

A similar numerical-experimental comparison is presented in Figure 20 for the models with the window opening. It can be observed that, also in this case, the load and drift capacity is captured accurately, and the model properly accounts for the influence of the compressive strength to the resistance. Furthermore, the rate of softening and the strength at the level of the ultimate displacement agree with the experimental observations. The comparison of the two types of specimens shows that the presence of the opening does not have a significant influence in the peak strength of the walls, but it increases the rate of strength degradation and reduces the initial ductility observed in the solid wall specimen, features accurately captured by the macroelement models.

Subsequently, the wall models have been subjected to cyclic loading, to investigate the ability of the macroelement model to reproduce the main features of the cyclic nonlinear behaviour. The resulting numerical curves for the solid wall specimens with σ_n=0.0 MPa and σ_n=0.1 MPa are shown in Figure 21, where they are compared against the experimental responses.

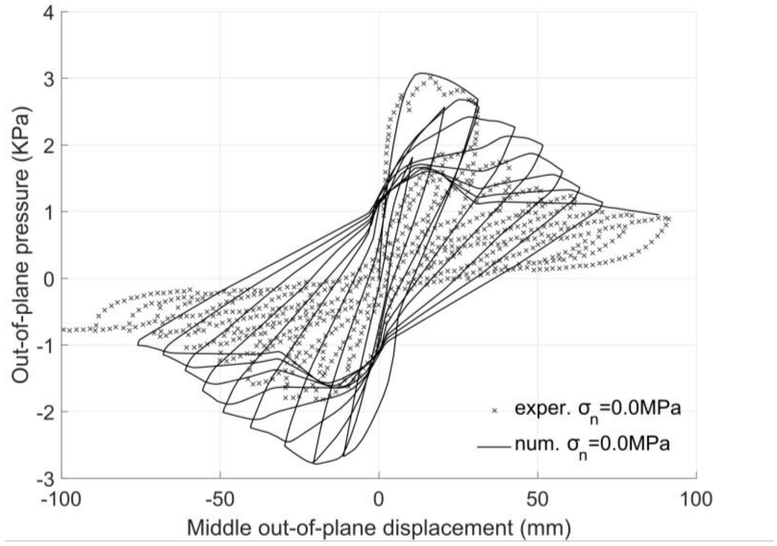

(a)

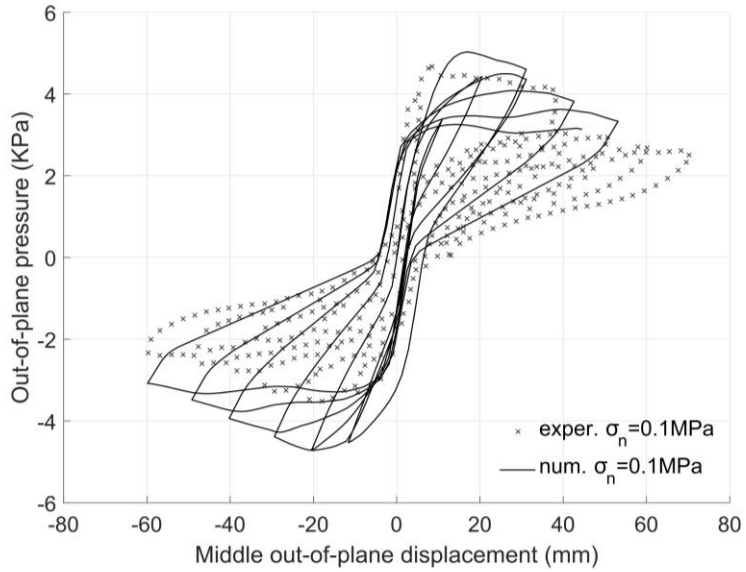

(b)

Figure 21. Numerical-experimental comparison for the solid walls out-of-plane loading: (a) σ_n=0.0 MPa, (b) σ_n=0.1 MPa

In both cases, the envelope of the cyclic response in the positive quadrant is in very close agreement with the experimental envelope; the load and out-of-plane drift capacity of the wall, as well as the rate of strength degradation are reproduced accurately. In the experimental curves reported by Griffith et al. [40], the strength upon load reversal appears significantly reduced, which is attributed to the pre-cracking of the wall up to +30 mm. This response characteristic is reproduced only to a small extent in the numerical analyses, which can be attributed to the characteristics of the constitutive law of Figure 10 employed for the out-of-plane springs. According to this material description, strength degradation develops separately in the positive and negative quadrants, thus the softening behaviour in one direction does not influence the response in the other direction. This assumption will be re-examined in future work.

Regarding the cracking pattern, indicative results for the solid wall with compressive stress σ_n=0.1 MPa are presented in Figure 22. Figure 22a displays the strength degradation in the out-of-plane springs, according to a colour-map which indicates the level of out-of-plane diagonal cracking. It can be observed that the damage of the out-of-plane springs of the main wall governs the response of the structure. The degraded springs are mainly the ones close to the corners, which correspond to the area where diagonal cracks first appeared during the experiments (Figure 22c). Figure 22b shows the deformed shape of the model at maximum positive displacement. The interfaces which develop significant damage are noted in the figure. The flexural damage along the horizontal interface at the top-centre of the wall corresponds to the horizontal crack along the bed joint in the centre of the experimental specimen (Figure 22c). Furthermore, sliding appears along the intersection of the main and the lateral walls, which is in good agreement with the experimental observations.

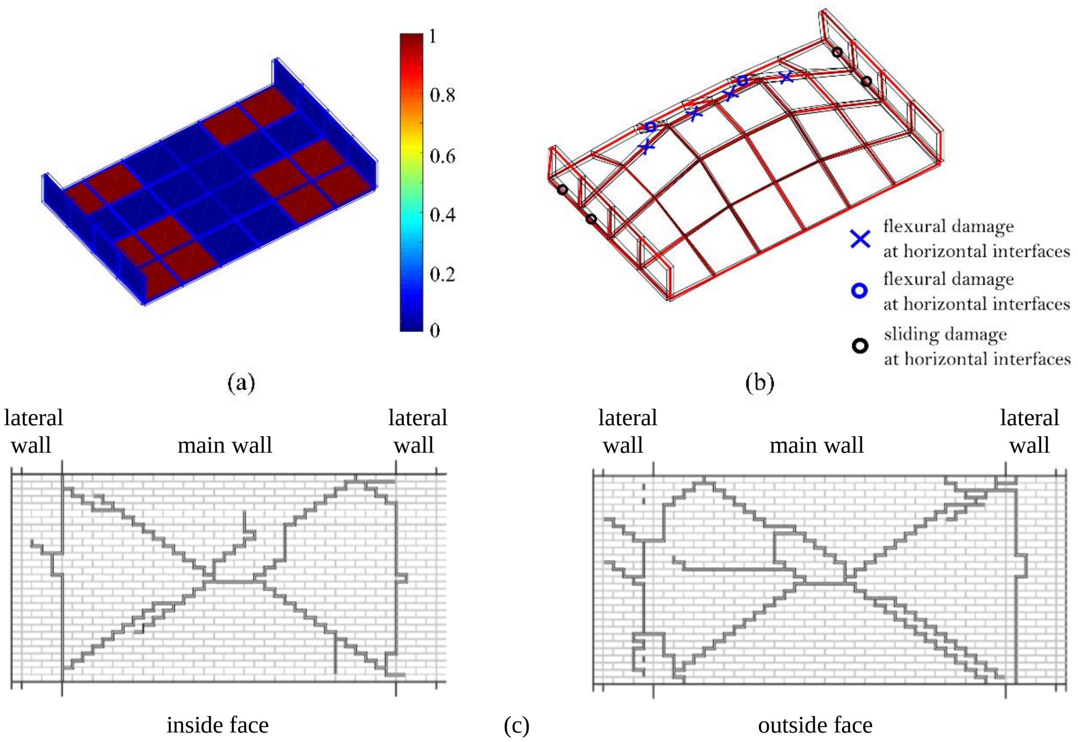

Figure 22. Solid wall σ_n=0.1MPa: (a) strength degradation of out-of-plane springs; (b) deformed shape at maximum displacement; (c) experimental cracking pattern [40]

Finally, Figure 23 shows the deformed shape and the strength degradation of the out-of-plane springs of the macroelements representing the response of the window wall specimen with σ_n=0.0 MPa under cyclic loading. Contrary to the solid wall specimens, where the diagonal out-of-plane damage was concentrated at the corners, in this case it is spread to all the macroelements of the main wall. This agrees with the outcome of the experimental test, which resulted in diffuse out-of-plane cracking along the main wall (Fig. 23c). Furthermore, the deformed shape of the model reveals a vertical crack at the top-centre of the masonry panel, which agrees with the experimental observations in the corresponding specimen (Fig. 23c). In addition, a horizontal crack has developed at the middle-right area which is also observed in the experimental cracking pattern in Fig. 23c.

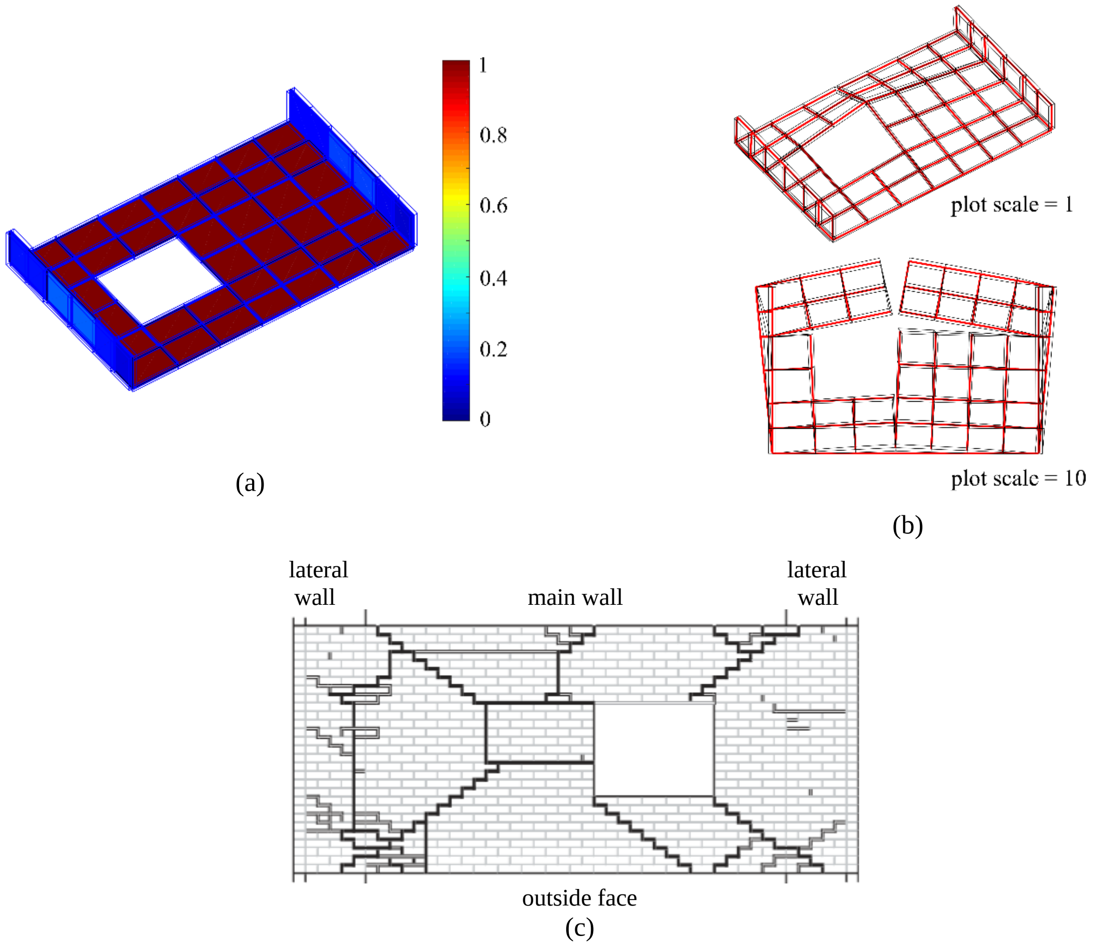

Figure 23. Window wall with σ_n=0.0 MPa: (a) strength degradation of out-of-plane springs; (b) deformed shape at maximum displacement; (c) experimental cracking pattern [40]

4.4 In-plane response of two-storey façade

This section investigates the ability of the macroelement model to accurately reproduce the behaviour of a large URM system, such as the two-storey perforated wall tested under in-plane cyclic loading by Magenes et al. [41]. The masonry wall was part of a full-scale brick-masonry building specimen built using a two-wythe English bond pattern and the same materials used in the experiments simulated in Section 4.2. Dead weights were placed at the two floor levels giving rise to a pre-compression of approximately 0.5 MPa to the bed joints at bottom of the walls. The structure was subjected to displacement control cyclic loading, with equal horizontal forces applied at each floor level in the direction shown in Fig. 24a. The analysed wall (*Wall D* in [41]) correspond to one of the two longitudinal faces of the building, which was not connected to the adjacent lateral walls. Hence the influence of the remaining structure on the in-plane response of this façade can be considered negligible and *Wall D* is modelled in isolation.

A macroelement model has been developed for *Wall D* using the mesh shown in Figure 24a. In the model, the nodes belonging to the macroelement edges along the bottom boundary are fully restrained, representing the rigid base. Equal forces are applied at floor levels and the displacement is controlled through a middle master node, using the configuration shown in Fig. 24b. The material properties of the models are the same as the properties defined for the macroelements in Section 4.2 which are reported in Tables 3 and 4.

The numerical response of the macroelement model in terms of in-plane displacement at the second floor with respect to the base shear force of Wall D is presented in Figure 25. The numerical curve is compared to the experimental response provided in [41], and a very close agreement can be observed between the two response curves. The load capacity is predicted within 10% accuracy, while the corresponding drift is also closely identified. Furthermore, the strength and stiffness degradation of the structure within the series of loading cycles is very well reproduced, allowing a realistic prediction of residual drifts and hysteretic energy dissipation.

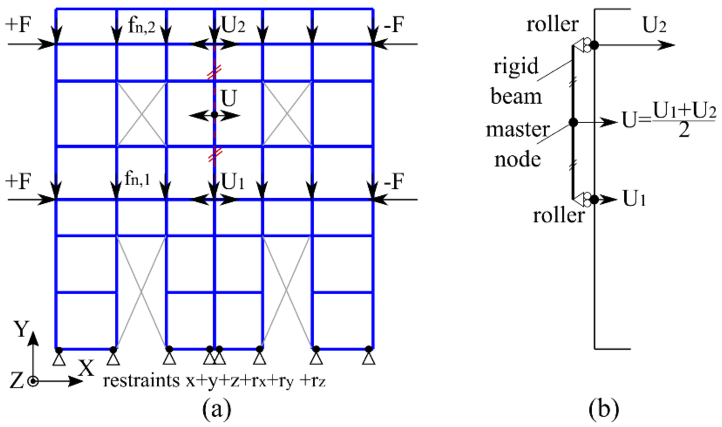

Figure 24. (a) Macroelement model of *Wall D*; (b) configuration for displacement control analysis with equal forces at floor levels

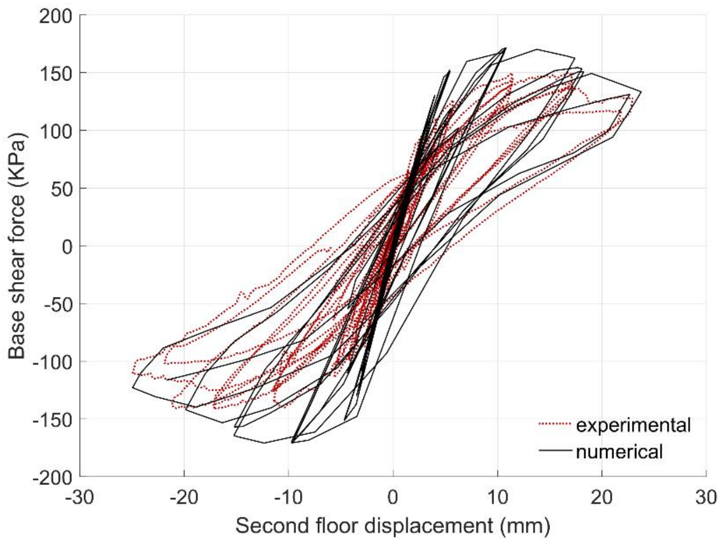

Figure 25. Two-storey URM façade: experimental-numerical comparison

In Fig. 26a, the deformed shape of the macroelement model at the point of the largest lateral drift is plotted, while Fig. 26b depicts the strength degradation of the in-plane shear springs at the end of the cyclic analysis. The failure pattern derived by these figures is in good agreement with the experimental observations (Fig. 26c). More specifically, the significant horizontal flexural cracks at the bases of the three piers and at the level of the second floor windows is effectively represented by the nonlinear interfaces at the edges of the macroelements (Fig. 26a), and shear failure in the two first floor spandrels and in the ground floor central pier is captured by in-plane diagonal springs (Fig. 26b). However, it should be noted that there are some discrepancies between the predicted and the observed damage patterns, mainly in the ground floor central pier where the adopted mesh of macroelements leads to underestimating the extent of shear damage. In any case, it should be stressed that the proposed modelling strategy with macroelements, due to its phenomenological nature, is not aimed at providing an accurate representation of the actual cracks in the brick-work, but at predicting the main response characteristics including strength and stiffness degradation under cyclic loading as shown in Fig. 25.

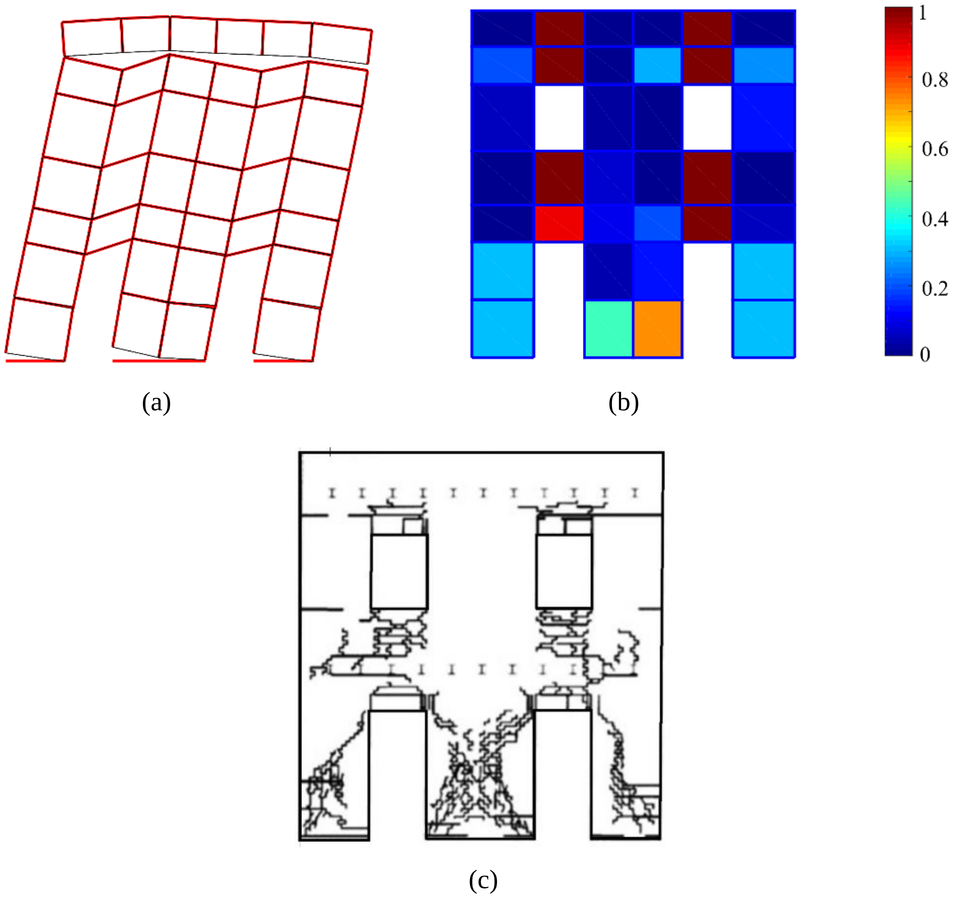

Figure 26. (a) Deformed shape of macroelement model at peak in-plane displacement; (b) strength degradation of diagonal shear springs at the end of the cyclic analysis; (c) experimental cracking pattern [41]

4.5 In-plane-response of concrete frame with masonry infill

The final application considered herein concerns the modelling of infill frames with the use of the macroelement for the representation of the URM parts of the system. This example allows the investigation of the alternative features of the macroelement kinematics, specifically developed to allow for the interaction with frames. More precisely, macroelements containing full-DOF edges are employed. Furthermore, the macroelements in contact with the corners of the frames include edges which share nodes, as explained in Section 2.2. The enhanced kinematics of the homogeneous block, including an out-of-plane diagonal bending mode, allows a better representation of the in-plane and out-of-plane failure modes compared to previous discrete element formulations as proposed in [31, 32].

An experimental test of single-storey reinforced concrete (RC) infill frames under in-plane loading [42], performed in the Construction Engineering Research Laboratory at Champaign (Illinois), is simulated and the results obtained numerically are compared against the experimental observations. The single-bay bare frame and brick-infill frame specimens are considered here. The geometric characteristics of the frame and the infill are shown in Fig. 27a. Details on the reinforcement can be found in [42]. The specimens were loaded in-plane at the storey level through the actuator sketched in Fig. 27a. The horizontal force was plotted against the top horizontal displacement in each case to assess the influence of the infill panel to the resistance of the frame.

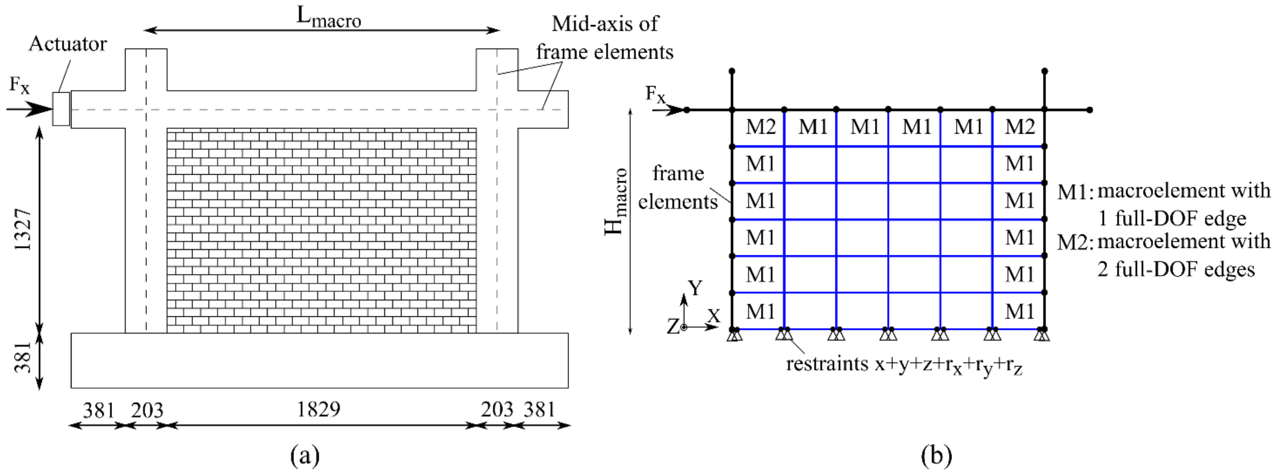

Figure 27. (a) Single-bay infill frame tested experimentally under in-plane loading [41]; (b) FE model with macroelements for masonry infill

In the numerical models developed in ADAPTIC [37], the frame is represented by means of two-noded cubic elasto-plastic beam elements with 6-DOFs per node. Each frame member is modelled with six beam elements, as shown in Fig. 27b to accurately represent the nonlinear response of the frame. A symmetric reinforced concrete section is utilised for the beam elements. The material behaviour of concrete is modelled using a constitutive law with a parabolic envelope in compression and a cap in tension with zero post-yield tensile stress, while the material behaviour of steel reinforcement is considered elastic-perfectly plastic. The material parameters for the frame, are presented in Table 6 and they are based on the material properties reported in [42].

Table 6. Material properties of concrete and steel reinforcement

Concrete				**Steel**	
f_c [MPa]	**f_t [MPa]**	**$\varepsilon_{c,0}$**	**w [KN/m^3]**	**E_s [GPa]**	**σ_y [MPa]**
38.5	1.5	0.2%	25.0	200.0	377.0

The wall panel of the brick-infill frame specimen is modelled employing macroelements. To achieve mesh compatibility with the frame - hence accurate representation of the interaction between macroelements and beam elements - a mesh of 6×6 macroelements is employed, as shown in Figure 27b. The edges of the macroelements that coincide with beam elements of the frame are defined as full-DOF edges. This allows the external edges to have the same deformed shape as the frame elements, which ensures accurate representation of the interaction between the frame and the block through the cohesive interfaces. The macroelements with one or two full-DOF edges are marked in Figure 27b. The remaining edges defining the boundaries between macroelements are reduced-DOF. All the macroelements are defined by 8 distinct nodes, except for the two elements at the corners of the infill panel, which include two consecutive full-DOF edges sharing the corner node of the frame. The material properties adopted for the shear spring and the cohesive interfaces at the boundaries of the macroelements are reported in Tables 7 AND 8. The properties corresponding to the macroscopic in-plane behaviour of the URM infill panel were already calibrated by Pantò et al. [42], who modelled the same experimental test with the 3D discrete macroelement proposed in [32]. Similar parameters are adopted in the macroelement model herein.

Table 7. Material parameters for macroelement cohesive interfaces

	Young's modulus E [N/mm^2]	Tensile strength f_t [N/mm^2]	Cohesion c [N/mm^2]	Friction angle $\tan\phi$	Fracture energy G_f [N/mm]	
					Mode I	Mode II
Horizontal	2500	0.15	0.30	0.40	0.05	0.10
Vertical	2000	0.60	0.70	0.50	0.05	0.10

Table 8. Material parameters for macroelement diagonal shear spring

Elastic shear modulus G_e [N/mm^2]	Post-peak shear modulus G_p [N/mm^2]	Shear strength at zero confinement $\tau_{Y,0}$ [N/mm^2]	Coefficient of friction μ_d
1000	-10	0.30	0.15

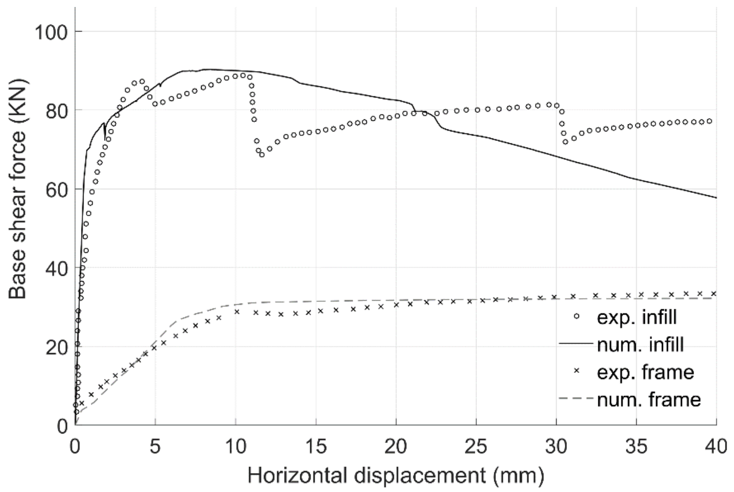

Figure 28. Numerical response of bare frame and infill frame model compared to the experimental response

At first, the bare frame specimen has been analysed under horizontal in-plane loading applied at the storey level, to verify the accurate representation of its nonlinear behaviour. The force – displacement curve is shown in Fig. 28 against the experimental curve [42]. A very close agreement between the numerical and the experimental curve is observed, which validates the modelling strategy chosen for the bare frame. Subsequently, the detailed infill frame model with a 6×6 macroelement mesh is analysed. The global behaviour of the coupled model in terms of horizontal force and top horizontal displacement is also shown in Fig. 28, where it is compared against the corresponding experimental curve. It can be observed that the influence of the infill panel in the initial stiffness, as well as the load capacity of the frame, is accurately reproduced. In the post-peak region, the tested specimen exhibits a behaviour characterised by abrupt drops in the strength followed by gradual partial recovery. Instead, the numerical curve shows a smooth softening post-peak behaviour that results in moderately lower residual strength compared to the experimental curve. This is possibly due to the approximation of the post-peak behaviour of the URM block under diagonal shear cracking by a linear curve (in the constitutive law of the diagonal shear springs). The linear curve is chosen to provide an approximation of the global strength degradation, but, obviously, it cannot reproduce the effects of local crack opening and re-closure, which produce the abrupt drops in the strength of a URM specimen under shear.

The deformed shape of the infill frame model at the end of the nonlinear analysis is shown in Fig. 29a, while Fig. 29b presents the strength degradation of the diagonal shear springs at the same point. The development of a diagonal shear cracking mode, starting from the second and fourth row of macroelements and propagating to the larger region, can be observed in the two figures. This agrees with the experimental cracking pattern of the infill panel at this level of horizontal drift (Fig. 29c), as described by Al-Chaar et al. [42]. In addition, a horizontal crack extending along the largest part of the panel's length is observed in Fig. 29a between the fifth and sixth row of macroelements, while cracks of smaller length are spread over the infill wall's area. These cracks in the interfaces between the macroelement blocks reproduce the large horizontal and smaller vertical cracks observed experimentally (Figure 29c). On the whole, it is observed that the developed macroelement strategy can accurately represent URM components interacting with frame elements, when the external edges of the former share the DOFs and follow the deformed shape of the latter. This shows the effectiveness of the full-DOF variation of the macroelement edges, which ensures the accurate representation of the relative displacements along the interface between the frame and the URM infill.

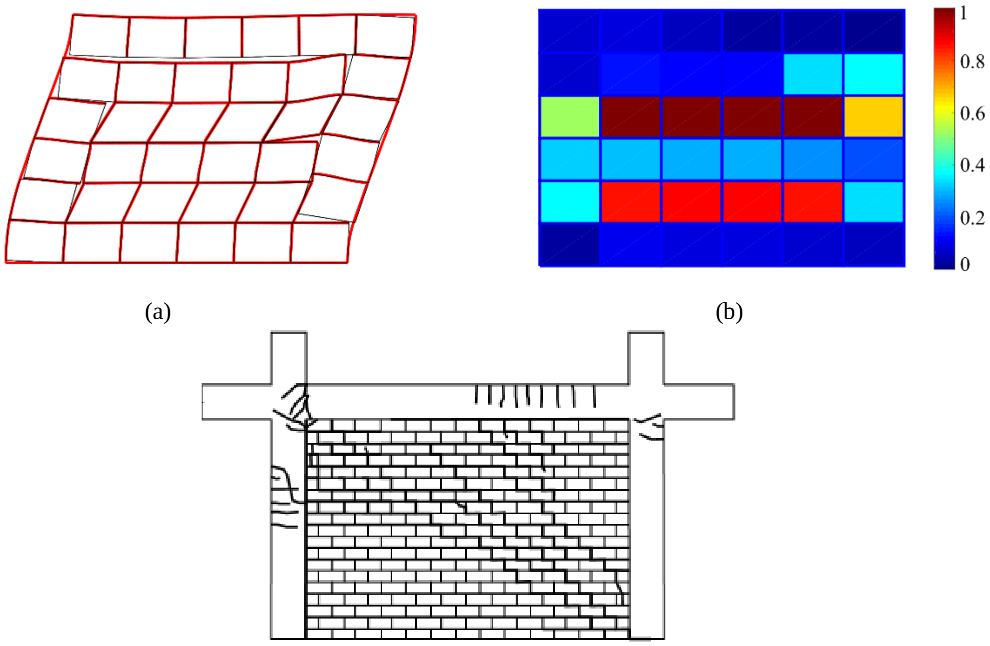

(a) (b)

(c)

Figure 29. Infill frame model at the end of the numerical analysis: (a) deformed shape; (b) strength degradation of diagonal shear springs; (c) experimental cracking pattern [42]

5 Concluding remarks

In this paper, a novel 3D macroelement for efficient and accurate nonlinear analysis of masonry structures is proposed. It is formulated within the FEM framework, adopting similar assumptions to previous discrete element representations of URM, with significant enhancements on the kinematic and material descriptions. Importantly, the proposed macroelement can represent the main in-plane and out-of-plane collapse mechanisms of URM panels. The flexural cracking, shear sliding and toe crushing failure modes are described allowing for their interaction through damage concentrated along the macroelement boundaries. The in-plane shear and out-of-plane diagonal cracking modes are represented in a phenomenological way by nonlinear springs associated with the respective deformation modes of the inner block. The constitutive behaviour of the springs is coupled with the mean normal stress in the boundary interfaces, which provides the level of confinement. The macroelement has a flexible connectivity along its four boundary edges and can therefore be used in combination with other finite elements with rotational freedoms including shell and beam elements. This is an important characteristic, as the proposed masonry macro-element description can be used not only to analyse masonry components in isolation, but also entire historical URM buildings, where the masonry elements interact with the floor systems, and modern infill frame structures, where the response up to collapse is governed by the complex interaction between masonry infill and surrounding frames. Numerical examples including comparisons against physical experiments have shown that:

- the enhanced kinematics in combination with the detailed cohesive-frictional constitutive law along the boundaries allow a reasonable representation of the in-plane and out-of-plane nonlinear behaviour of URM components;
- reliable predictions of failure modes can be achieved using a reduced number of elements for modelling solid walls, components (e.g. piers and spandrels) of large perforated walls and infill panels of framed structures;
- the proposed modelling strategy with macroelements enables an accurate prediction of the main response characteristics of masonry components including strength and stiffness degradation and hysteretic energy dissipation.

As a result, the proposed macroelement strategy offers a good balance between accuracy and efficiency for the 3D modelling of URM structures under monotonic and cyclic loading conditions. Further research will focus on extending the macroelement description to allow for geometric nonlinearity, which may affect the out-of-plane response under extreme loading conditions. Additionally, a consistent multiscale calibration strategy will be developed, where the macromodel material parameters are determined as a function of the actual masonry bond, the mechanical properties of the masonry constituents and the mesh characteristics of macroelement representation for typical masonry wall components.

References

[1] Lourenço, P. B. and Rots, J. G., 1997. Multisurface Interface Model for Analysis of Masonry Structures. Journal of Engineering Mechanics, 123(7): 660-668.

[2] Gambarotta, L. and Lagomarsino, S., 1997. Damage models for the seismic response of brick masonry shear walls. Part I: the mortar joint model and its applications. Earthquake Engineering and Structural Dynamics, 26(4): 423-439.

[3] Macorini, L. and Izzuddin, B., 2011. A non-linear interface element for 3D mesoscale analysis of brick-masonry structures. International Journal for numerical methods in Engineering, 85(12): 1584-1608.

[4] Lemos, J. V., 2007. Discrete element modeling of masonry structures. International Journal of Architectural Heritage, 1,2:190-213.

[5] Bui ,T.T., Limam, A., V. Sarhosis, V. and Hjiaj, M. 2017. Discrete element modelling of the in-plane and out-of-plane behaviour of dry-joint masonry wall constructions. Engineering Structures, 136:277–294.

[6] Malomo, D., De Jong, M.J. and Penna, A., 2019. Distinct element modelling of the in-plane cyclic response of URM walls subjected to shear-compression. Earthquake Engng Struct Dyn., (48):1322–1344.

[7] CUR Report 171, 1997. Structural masonry: an experimental/ numerical basis for practical design rules, (Ed. Rots, J.G), AA Balkema.

[8] Chisari, C., Macorini, L., Amadio, C. and Izzuddin, B., 2018. Identification of mesoscale model parameters for brick-masonry. International Journal of Solids and Structures, (146): 224-240.

[9] Jokhio, G.A. and Izzuddin, B.A., 2015. A Dual Super-Element Domain Decomposition Approach for Parallel Nonlinear Finite Element Analysis. International Journal for Computational Methods in Engineering Science and Mechanics, 16(3): 188-212.

[10] Macorini, L. and Izzuddin, B., 2013. Nonlinear analysis of masonry structures using mesoscale partitioned modelling. Advances in engineering Software, 60: 58-69.

[11] Massart, T., Peerlings, R. and Geers, M., 2007. An enhanced multi-scale approach for masonry wall computations with localization of damage. International journal for numerical methods in engineering, 69(5):1022-1059.

[12] Addessi, D. and Sacco, E., 2012. A multi-scale enriched model for the analysis of masonry panels. International Journal of Solids and Structures, 49(6):865-880.

[13] Leonetti, L., Greco, F., Trovalusci, P., Luciano, R. and Masiani, R., 2018. A multiscale damage analysis of periodic composites using a couple-stress/Cauchy multidomain model: Application to masonry structures, Composites Part B: Engineering, (141):50-59.

[14] Corradi, M., Borri, A. and Vignoli, A. 2003. Experimental study on the determination of strength of masonry walls. Construction and Building Materials, (17):325–337.

[15] Anthoine, A., 1995. Derivation of the in-plane elastic characteristics of masonry through homogenization theory. Int. J. Solids Struct., (32):137-163.

[16] Casolo, S., 2006. Macroscopic modelling of structured materials: Relationship between orthotropic Cosserat continuum and rigid elements. Int. J. Solids Struct., (43):475-496

[17] Silva, L., Lourenco, P. and Milani, G., 2018. Derivation of the out-of-plane behaviour of masonry through homogenization strategies: micro-scale level. Comput. Struct., (209):30-43.
[18] Chisari, C., Macorini, L., and Izzuddin B.A. 2020. Multiscale model calibration by inverse analysis for nonlinear simulation of masonry structures under earthquake loading. International Journal for Multiscale Computational Engineering, DOI: 10.1615/IntJMultCompEng.2020031740.
[19] Berto, L., Saetta, A., Scotta, R. and Vitaliani, R., 2002. An orthotropic damage model for masonry structures. International Journal for Numerical Methods in Engineering, 55(2): 127-157.
[20] Lourenço, P.B., Rots, J.G. and Blaauwendraad, J., 1998. Continuum model for masonry: parameter estimation and validation. Journal of Structural Engineering, 124(6): 642-652.
[21] Saloustros, S., Pelà, L., Cervera, M. and Roca, P., 2018. An enhanced finite element macro-model for the realistic simulation of localized cracks in masonry structures: A large-scale application. International Journal of Architectural Heritage, 12(3): 432-447.
[22] Brencich, A., Gambarotta, L. and Lagomarsino, S., 1998. A macroelement approach to the three-dimensional seismic analysis of masonry buildings, 11th European Conference on Earthquake Engineering, 6-11.
[23] Lagomarsino, S., Penna, A., Galasco, A. and Cattari, S., 2013. TREMURI program: an equivalent frame model for the nonlinear seismic analysis of masonry buildings. Engineering Structures, 56: 1787-1799.
[24] Magenes, G. and Fontana, A., 1998. Simplified non-linear seismic analysis of masonry buildings, Proc. Br. Masonry Soc., 8: 190-195.
[25] Rinaldin, G., Amadio, C. and Macorini, L., 2016, A macro-model with nonlinear springs for seismic analysis of URM buildings, Earthquake Engineering & Structural Dynamics, 45: 2261-228.
[26] Foraboschi, P. and Vanin, A., 2013. Non-linear static analysis of masonry buildings based on a strut-and-tie modeling. Soil Dynamics and Earthquake Engineering, 55: 44-58.
[27] Casolo, S. and Pena, F., 2007. Rigid element model for in-plane dynamics of masonry walls considering hysteretic behaviour and damage. Earthquake engineering & structural dynamics, 36(8): 1029-1048.
[28] Bertolesi, E., Milani, G. and Lourenço, P.B., 2016. Implementation and validation of a total displacement non-linear homogenization approach for in-plane loaded masonry. Computers & Structures, 176: 13-33.
[29] Silva, L.C., Lourenço, P.B. and Milani, G., 2017. Nonlinear Discrete Homogenized Model for Out-of-Plane Loaded Masonry Walls. Journal of Structural Engineering, 143(9): 04017099.
[30] Caliò, I., Marletta, M. and Pantò, B., 2012. A new discrete element model for the evaluation of the seismic behaviour of unreinforced masonry buildings. Engineering Structures, 40: 327-338.
[31] Pantò, B., Cannizzaro, F., Caddemi, S. and Caliò, I., 2016. 3D macro-element modelling approach for seismic assessment of historical masonry churches. Advances in Engineering Software, 97: 40-59.
[32] Pantò, B., Cannizzaro, F., Calio, I. and Lourenco, P., 2017. Numerical and Experimental Validation of a 3D Macro-Model for the In-Plane and Out-Of-Plane Behaviour of Unreinforced Masonry Walls. International Journal of Architectural Heritage, 11: 946-964.
[33] Minga, E., Macorini, L. and Izzuddin, B.A., 2018. A 3D mesoscale damage-plasticity approach for masonry structures under cyclic loading. Meccanica, 53: 1591–1611.
[34] Magenes, G. and Calvi, G.M., 1997. In-plane seismic response of brick masonry walls. Earthquake engineering & structural dynamics, 26(11): 1091-1112.
[35] Mann, W. and Muller, H., 1982. Failure of shear-stressed masonry. An enlarged theory, tests and application to shear walls, Proc. Br. Ceram. Soc., pp. 223.
[36] Zhang, S. and Beyer, K., 2019. Numerical investigation of the role of masonry typology on shear strength. Engineering Structures, (192): 86-102.
[37] Izzuddin, B.A., 1991. Nonlinear dynamic analysis of framed structures, Imperial College London (University of London).
[38] Anthoine, A., Magonette, G. and Magenes, G., 1995. Shear-compression testing and analysis of brick masonry walls, Proceedings of the 10th European conference on earthquake engineering, 1657-1662.
[39] Minga, E., 2017. 3D Meso- and Macro-scale models for nonlinear analysis of masonry systems, Imperial College London.
[40] Griffith, M.C., Vaculik, J., Lam, N., Wilson, J. and Lumantarna, E., 2007. Cyclic testing of unreinforced masonry walls in two-way bending. Earthquake Engineering & Structural Dynamics, 36(6): 801-821.
[41] Magenes, G., Kingsley, G.R. and Calvi, G.M., 1995. Seismic testing of a full-scale, two-story masonry building: test procedure and measured experimental response. From the Report: Experimental and numerical investigation on a brick masonry building prototype - numerical prediction of the experiment, Report 3.0 - GNDT, University of Pavia (Italy).
[42] Al-Chaar, G., Issa, M. and Sweeney, S., 2002. Behavior of masonry-infilled nonductile reinforced concrete frames. Journal of Structural Engineering, 128(8): 1055-1063.
[43] Panto, B., Calio, I., Lourenco, P.B., 2018, A 3D discrete macro-element for modelling the out-of-plane behaviour of infilled frame structures, Engineering Structures, 175: 371-385.

Appendix A: Interpolation of external edge displacement field

Let xyz be the local reference system of an external edge of the macroelement, as shown in Figure 6. The vector containing the basic DOFs of the two nodes defining a specific edge (i), $i = 1{:}\,4$, expressed in the local system of the edge is noted as $\boldsymbol{u_{s,i}}$. For a reduced-DOF edge:

$$\boldsymbol{u_{s,i}} = \begin{bmatrix} u_{x,0} & u_{y,0} & u_{z,0} & \theta_{x,0} & \theta_{y,0} & \theta_{z,0} & u_{x,L} & u_{y,L} & u_{z,L} & \theta_{x,L} & \theta_{y,L} & \theta_{z,L} \end{bmatrix}^T \tag{38}$$

while for a full-DOF edge:

$$\boldsymbol{u_{s,i}} = \begin{bmatrix} u_{x,0} & u_{y,0} & u_{z,0} & \theta_{x,0} & u_{x,L} & u_{y,L} & u_{z,L} & \theta_{x,L} \end{bmatrix}^T \tag{39}$$

The DOFs with the subscript $*_{,0}$ refer to the node at $x = 0$, while the ones with the subscript $*_{,L}$ refer to the node at $x = L$. The vector $\boldsymbol{u_{s,i}}$ can be extracted by the element nodal DOF vector $\boldsymbol{U_s}$. The transformation is performed through a transformation matrix $\boldsymbol{T_{s,i}}$ which is constant in the case of small displacements examined here:

$$\boldsymbol{u_{s,i}} = \boldsymbol{T_{s,i}}\,\boldsymbol{U_s} \tag{40}$$

The cohesive interface defined along the boundary is a 2D zero-thickness interface, as illustrated in Figure 6. An isoparametric space (ξ, η) with $\xi \in [-1 \;\; 1]$ and $\eta \in [-1 \;\; 1]$ is defined for the interface mid-surface, as shown in Figure 30. The natural coordinates (ξ, η) will be used in the definition of the variable fields in the following.
Let $\boldsymbol{u_{ed,i}}(\xi)$ be the displacement and rotation field along the external edge (i), $i = 1{:}\,4$, interpolated by the DOFs in $\boldsymbol{u_{s,i}}$ using standard beam shape functions, linear for a reduced-DOF edge and quadratic for a full-DOF edge.
For a reduced-DOF edge:

$$\boldsymbol{u_{ed,i}}(\xi) = \begin{bmatrix} u_x^{ed,i}(\xi) & u_y^{ed,i}(\xi) & u_z^{ed,i}(\xi) & \theta_x^{ed,i}(\xi) \end{bmatrix}^T \tag{41}$$

while for a full-DOF edge:

$$\boldsymbol{u_{ed,i}}(\xi) = \begin{bmatrix} u_x^{ed,i}(\xi) & u_y^{ed,i}(\xi) & u_z^{ed,i}(\xi) & \theta_x^{ed,i}(\xi) & \theta_y^{ed,i}(\xi) & \theta_z^{ed,i}(\xi) \end{bmatrix}^T \tag{42}$$

The external side of the cohesive interface is a 2D extension of the two-noded edge, as shown in Figure 6. The displacement field along the 2D external side of the interface is noted as $\boldsymbol{u_{ext,i}}(\xi, \eta) = \begin{bmatrix} u_x^{ext,i}(\xi, \eta) & u_y^{ext,i}(\xi, \eta) & u_z^{ext,i}(\xi, \eta) \end{bmatrix}$, $i = 1{:}\,4$, and can be estimated by the following equations:

$$u_x^{ext,i}(\xi, \eta) = u_x^{ed,i}(\xi) + \frac{W\eta}{2}\theta_y^{ed,i}(\xi) \tag{43}$$

$$u_y^{ext,i}(\xi, \eta) = u_y^{ed,i}(\xi) + \frac{W\eta}{2}\theta_x^{ed,i}(\xi) \tag{44}$$

$$u_z^{ext,i}(\xi, \eta) = u_z^{ed,i}(\xi) \tag{45}$$

In case of a reduced-DOF edge, $\theta_y^{ed,i}$ is constant along the edge and can be obtained by:

$$\theta_y^{ed,i} = \frac{u_{z,0} - u_{z,L}}{L_i} \tag{46}$$

The displacement field $\boldsymbol{u_{ext,i}}$ is expressed in the local reference system xyz of edge (i).

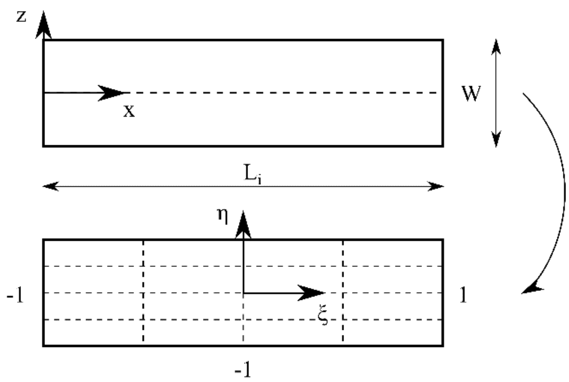

Figure 30. Isoparametric space corresponding to the mid-surface of a zero-thickness interface

Equations (43)-(45) can be written in matrix form as follows:

$$\boldsymbol{u_{ext,i}}(\xi,\eta) = \boldsymbol{N_s}(\xi,\eta)\,\boldsymbol{u_{s,i}} = \boldsymbol{N_s}(\xi,\eta)\,\boldsymbol{T_{s,i}}\,\boldsymbol{U_{s,i}} \tag{47}$$

where $\boldsymbol{N_s}(\xi,\eta)$ is the matrix containing the shape functions for the interpolation of the displacements along the external surface of interface (i), by the DOFs in $\boldsymbol{u_{s,i}}$. For a reduced-DOF edge, matrix $\boldsymbol{N_s}(\xi)$ is written as follows:

$$\boldsymbol{N_s}(\xi,\eta) = \begin{bmatrix} N_{u_{x,0}} & 0 & \frac{W\eta}{2L_i} & 0 & N_{u_{x,L}} & 0 & -\frac{W\eta}{2L_i} & 0 \\ 0 & N_{u_{y,0}} & 0 & 0 & 0 & N_{u_{y,L}} & 0 & 0 \\ 0 & 0 & N_{u_{z,0}} & 0 & 0 & 0 & N_{u_{z,L}} & 0 \end{bmatrix} \tag{48}$$

where:

$$N_{u_{x,0}} = N_{u_{y,0}} = N_{u_{z,0}} = \frac{1}{2}(1-\xi) \tag{49}$$

$$N_{u_{x,L}} = N_{u_{y,L}} = N_{u_{z,L}} = \frac{1}{2}(1+\xi) \tag{50}$$

For a full-DOF edge, matrix $\boldsymbol{N_s}(\xi,\eta)$ has the form:

$$\boldsymbol{N_s} = \begin{bmatrix} N_{u_{x,0}} & 0 & \frac{W\eta}{2L_i}N'_{u_{z,0}} & 0 & \frac{W\eta}{2}N'_{\theta_{y,0}} & 0 & \cdots \\ 0 & N_{u_{y,0}} & 0 & -\frac{W\eta}{2}N_{\theta_{x,0}} & 0 & N_{\theta_{z,0}} & \cdots \\ 0 & 0 & N_{u_{z,0}} & 0 & N_{\theta_{y,0}} & 0 & \cdots \end{bmatrix.$$
$$\begin{matrix} \cdots & N_{u_{x,L}} & 0 & \frac{W\eta}{2L_i}N'_{u_{z,L}} & 0 & \frac{W\eta}{2}N'_{\theta_{y,L}} & 0 \\ \cdots & 0 & N_{u_{y,L}} & 0 & -\frac{W\eta}{2}N_{\theta_{x,L}} & 0 & N_{\theta_{z,L}} \\ \cdots & 0 & 0 & N_{u_{z,L}} & 0 & N_{\theta_{y,L}} & 0 \end{matrix}\Bigg] \tag{51}$$

where:

$$N_{u_{x,l}} = N_{\theta_{x,l}} = \frac{1}{2}(1-\xi) \tag{52}$$

$$N_{u_{y,l}} = N_{u_{z,l}} = \frac{1}{4}(1-\xi)^2(2+\xi) \tag{53}$$

$$N_{\theta_{y,l}} = N_{\theta_{z,l}} = \frac{L}{8}(1-\xi)^2(1+\xi) \tag{54}$$

$$N_{u_{x,r}} = N_{\theta_{x,r}} = \frac{1}{2}(1+\xi) \tag{55}$$

$$N_{u_{y,r}} = N_{u_{z,r}} = \frac{1}{4}(1+\xi)^2(2-\xi) \tag{56}$$

$$N_{\theta_{y,r}} = N_{\theta_{z,r}} = \frac{L}{8}(1+\xi)^2(\xi-1) \tag{57}$$

From Equation (47), the following expression can be derived for matrix $\boldsymbol{N_{s,i}}$ used in Equation (6):

$$\boldsymbol{N_{s,i}} = \boldsymbol{N_s}\,\boldsymbol{T_{s,i}} \tag{58}$$

Appendix B: Interpolation of block face displacement field

Let $\boldsymbol{u_{int,i}}(\xi,\eta) = \left[u_x^{int,i}(\xi,\eta) \quad u_y^{int,i}(\xi,\eta) \quad u_z^{int,i}(\xi,\eta)\right]^T$ be the displacement field along the face of the block that constitutes the internal side of the cohesive interface (i), $i = 1{:}\,4$. The field $\boldsymbol{u_{int,i}}$ is expressed in the local reference system of edge (i) and is interpolated by the seven additional DOFs depicted in Figure 31. The additional DOFs in the latter figure are expressed in the local reference system xyz and will be referred to as local additional DOFs of interface (i). Let $\boldsymbol{u_{a,i}} = [a_1, \ldots, a_7]^T$ be the vector containing the local additional DOFS of interface (i). The vector $\boldsymbol{u_{a,i}}$ can be obtained from vector $\boldsymbol{U_a}$ of the element additional DOFs through a transformation matrix $\boldsymbol{T_{a,i}}$ consisting of 0, 1 and -1 elements:

$$\boldsymbol{u_{a,i}} = \boldsymbol{T_{a,i}}\,\boldsymbol{U_a} \tag{59}$$

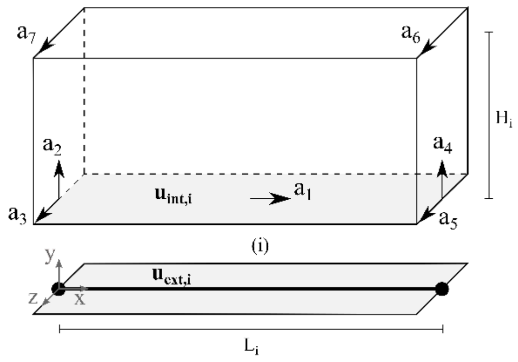

Figure 31. Local additional DOFs of interface (i)

The displacement field along the internal side of the interface is noted as:

$$\boldsymbol{u_{int,i}}(\xi,\eta) = \left[u_x^{int,i}(\xi,\eta) \quad u_y^{int,i}(\xi,\eta) \quad u_z^{int,i}(\xi,\eta)\right], \quad i = 1{,}4 \tag{60}$$

and can be estimated by the following equation:

$$\boldsymbol{u_{int,i}}(\xi,\eta) = \boldsymbol{N_a}(\xi,\eta)\,\boldsymbol{u_{a,i}} = \boldsymbol{N_a}(\xi,\eta)\,\boldsymbol{T_{a,i}}\,\boldsymbol{U_a} \tag{61}$$

where:

$$\boldsymbol{N_a} = \begin{bmatrix} 1 & \frac{W\eta}{2L_i} & 0 & -\frac{W\eta}{2L_i} & \ldots \\ 0 & 0 & \frac{1}{2}(1-\xi) + \frac{W\eta}{4H_i}(1-\xi) & 0 & \ldots \\ 0 & \frac{1}{2}(1-\xi) & 0 & \frac{1}{2}(1+\xi) & \ldots \end{bmatrix}$$

$$\begin{matrix} \ldots & 0 & 0 & 0 \\ \ldots & \frac{1}{2}(1+\xi) + \frac{W\eta}{4H_i}(1+\xi) & -\frac{W\eta}{2H_i}(1+\xi) & -\frac{W\eta}{2H_i}(1-\xi) \\ \ldots & \frac{1}{2}(1+\xi) & 0 & 0 \end{matrix} \Bigg] \tag{62}$$

Taking into account Equation (47), the matrix $\boldsymbol{N_{a,i}}$ used in Equation (6) can be written as:

$$\boldsymbol{N_{a,i}} = \boldsymbol{N_a}\,\boldsymbol{T_{a,i}} \tag{63}$$